Earth Syst. Sci. Data, 14, 5573–5603, 2022
https://doi.org/10.5194/essd-14-5573-2022

Open Access Earth System Science Data

Global climate-related predictors at kilometer resolution for the past and future

Philipp Brun[1], **Niklaus E. Zimmermann**[1], **Chantal Hari**[1,2,3], **Loïc Pellissier**[1,4], **and Dirk Nikolaus Karger**[1]

[1]Land Change Science, Swiss Federal Research Institute WSL, 8903 Birmensdorf, Switzerland
[2]Climate and Environmental Physics, Physics Institute, University of Bern, 3012 Bern, Switzerland
[3]Oeschger Centre for Climate Change Research, University of Bern, 3012 Bern, Switzerland
[4]Ecosystems and Landscape Evolution, Institute of Terrestrial Ecosystems, Department of Environmental System Science, ETH Zürich, 8092 Zürich, Switzerland

Correspondence: Philipp Brun (philipp.brun@wsl.ch)

Received: 17 June 2022 – Discussion started: 27 June 2022
Revised: 4 November 2022 – Accepted: 20 November 2022 – Published: 16 December 2022

Abstract. A multitude of physical and biological processes on which ecosystems and human societies depend are governed by the climate, and understanding how these processes are altered by climate change is central to mitigation efforts. We developed a set of climate-related variables at as yet unprecedented spatiotemporal detail as a basis for environmental and ecological analyses. We downscaled time series of near-surface relative humidity (hurs) and cloud area fraction (clt) under the consideration of orography and wind as well as near-surface wind speed (sfcWind) using the delta-change method. Combining these grids with mechanistically downscaled information on temperature, precipitation, and solar radiation, we then calculated vapor pressure deficit (vpd), surface downwelling shortwave radiation (rsds), potential evapotranspiration (pet), the climate moisture index (cmi), and site water balance (swb) at a monthly temporal and 30 arcsec spatial resolution globally from 1980 until 2018 (time-series variables). At the same spatial resolution, we further estimated climatological normals of frost change frequency (fcf), snow cover days (scd), potential net primary productivity (npp), growing degree days (gdd), and growing season characteristics for the periods 1981–2010, 2011–2040, 2041–2070, and 2071–2100, considering three shared socioeconomic pathways (SSP126, SSP370, SSP585) and five Earth system models (projected variables). Time-series variables showed high accuracy when validated against observations from meteorological stations and when compared to alternative products. Projected variables were also highly correlated with observations, although some variables showed notable biases, e.g., snow cover days. Together, the CHELSA-BIOCLIM+ dataset presented here (https://doi.org/10.16904/envidat.332, Brun et al., 2022) allows improvement to our understanding of patterns and processes that are governed by climate, including the impact of recent and future climate changes on the world's ecosystems and the associated services on societies.

1 Introduction

Climate change is impacting multiple facets of the Earth system, with consequences for the functioning of natural ecosystems, for the persistence of biological diversity, and for human societies (IPCC, 2022; IPBES, 2018). Climate regulates a broad variety of processes on Earth. It feeds, for example, rivers with precipitation, it generates wind, which is critical for renewable energy production (IPCC, 2011), and it fuels ecosystem and agricultural productivity (Howden et al., 2007), which sustains nearly all life on Earth, including humans (Bellard et al., 2012; Araújo and Rahbek, 2006; Willis and Bhagwat, 2009). Many of these processes react sensibly to climate change (IPCC, 2022), and in order to mitigate negative impacts, a sound understanding of the underlying relationships is key. Among the impacts of climate change are, for example, recent droughts and associated dis-

turbances, such as forest diebacks (Allen et al., 2010), which have fostered studies that attempted to identify and characterize the responsible climate signatures (Seneviratne et al., 2012; Zscheischler et al., 2018). Most of these disruptive events can only be detected and analyzed at high spatial and/or temporal resolutions and within a restricted area and period (Easterling et al., 2000). In many regions of the world, existing climate time series lack such high resolution and thus only to a limited degree allow establishment of an understanding of how climate interacts with the natural and human system (Easterling et al., 2016). By the end of the 21st century climate change is expected to lead to profound changes in the distribution ranges of species and ecosystems (Thuiller et al., 2005, 2019). A reasonable anticipation of such changes must rely on sound information on climate-related variables, considering different climate-change scenarios at an informative spatial and temporal resolution. The availability of relevant climate-related data at high spatiotemporal resolution for current conditions and for the decades ahead of us is therefore crucial for filling the gaps in our understanding of climate-change impact on the Earth system.

A popular repository for climate data is hosted by the climatologies at high resolution for the Earth's land surface areas (CHELSA) initiative (Karger et al., 2017, 2020, 2021b), which provides information on temperature and precipitation globally at kilometer resolution. Originally, the CHELSA initiative offered climate data primarily as climatologies, i.e., as monthly and seasonal statistics typically averaged over a representative period of 30 years or longer (Arguez and Vose, 2011), initially from 1979 to 2013. A key set of such climatologies comprises the 19 bioclimatic variables (Hijmans et al., 2005) that represent seasonal and annual statistics of precipitation and temperature and are widely used as predictors in macroecology (Fourcade et al., 2018). However, while these original data may be relevant for many applications, they have three primary limitations: they only (1) include variables that independently summarize either temperature or precipitation, (2) represent long-term climatic conditions, and (3) represent the recent past.

For a sound understanding of how physical and biological processes are driven by climate, information on temperature and precipitation alone is not sufficient. Assessing the potential for solar energy production, for example, is impossible without knowing how much shortwave solar radiation reaches a location of interest. Similarly, precipitation may measure the amount of water that reaches the surface, but across the globe this is an inaccurate proxy for the amount of water that is available to plants: $300\,\mathrm{kg\,m^{-2}}$ annual precipitation, for instance, can be found in the Alaskan taiga, in the Mongolian steppe, or in the Pakistani desert (Karger et al., 2017), where the dominant vegetation exhibits large differences in the ability to cope with water stress. Across these systems a much more accurate indicator of water stress is the climate moisture index (cmi, Hogg, 1997), i.e., the difference between precipitation and potential evapotranspiration (pet), as pet differs by a factor of 3 between the Alaskan taiga and the Pakistani desert (Singer et al., 2021). The popularity of the 19 bioclimatic variables to summarize climate therefore appears to result rather from the lack of relevant alternatives with kilometer resolution than from their imminent relevance.

Time-series data on climate-related variables are indispensable for understanding the drivers of the many important Earth system processes that vary with time. Resolving how the primary weather patterns unfold, for example, allows for a much deeper understanding of the control of spatiotemporal patterns of ecosystem productivity (Hartman et al., 2020). Similarly, time series of pet and cmi can be used to understand the country-wide temporal dynamics in crop yield (Zhang et al., 2015; Santini et al., 2022). Modeling crop yields based on sound pet and cmi data may, in turn, allow for a better anticipation of shortages in food production and agricultural planning. Moreover, extreme weather anomalies such as droughts can be identified at large scales and better linked to consequential disturbances like wildfires and forest diebacks. While for temperature and precipitation such time series of high temporal (daily) resolution data have recently been published (Karger et al., 2020, 2021b), global time series at kilometer resolution are hardly available for additional climate-related variables relevant to understanding ecosystem processes.

In order to anticipate and mitigate the manifold impacts of climate change until the end of this century, future projections of meaningful climate-related variables are required. Climate change is expected to continue or even accelerate in the coming decades, and its impacts on ecosystems and human societies are likely becoming stronger (IPCC, 2022). Crop yields, for example, are expected to change, tracking their optimal climate (Leng and Hall, 2019; IPCC, 2022): at high latitudes, harvests may become bigger due to warming, whereas elsewhere irrigation may become necessary to keep growing traditional crops (Liu et al., 2021; Masia et al., 2021). In certain areas some crops will likely have to be abandoned entirely and replaced with better-adapted alternatives (Sloat et al., 2020). Such agricultural system changes are costly, take time, and are only efficient if the expected changes can be reasonably well anticipated. Similarly, coping with the ongoing biodiversity crisis requires a rapid establishment of an optimally designed global network of protected areas (Elsen et al., 2020; Hannah, 2008; Pollock et al., 2017). However, finding the most sustainable way of creating such a network requires knowledge of the expected changes in climate and their impacts on the distribution ranges of species. For temperature and precipitation, high-resolution future climatologies have been made available (Karger et al., 2017), but this is generally not the case for other climate-related variables that are more directly linked to ecosystem processes.

Here, we present the CHELSA-BIOCLIM+ (climatologies at high resolution for the Earth's land surface areas

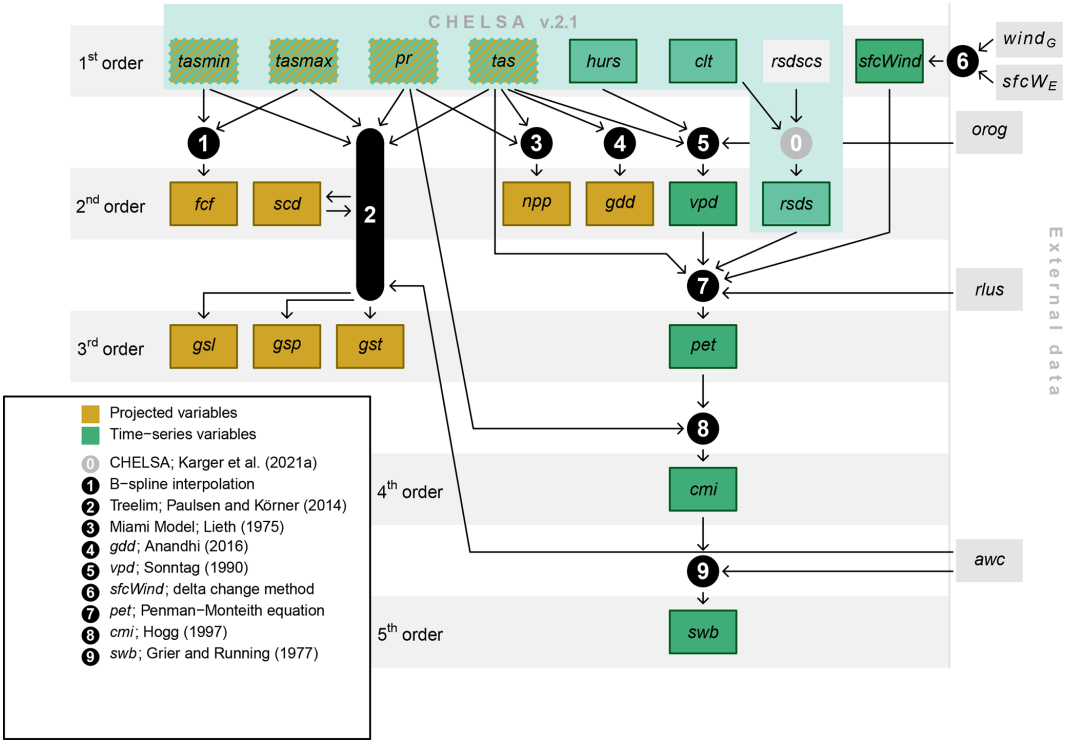

Figure 1. Input data, analyses, and output variables generated. tasmin represents daily minimum near-surface air temperature; tasmax represents daily maximum near-surface air temperature; pr represents precipitation rates; tas represents near-surface daily average air temperature; hurs represents near-surface relative humidity; clt represents cloud area fraction; rsdscs represents surface downwelling shortwave radiation assuming clear sky; orog represents orography; fcf represents frost change frequency; scd represents snow cover days; npp represents potential net primary productivity; gdd represents growing degree days; vpd represents vapor pressure deficit; rsds represents surface downwelling shortwave radiation corrected for atmospheric transmissivity and topography; sfcWind represents near-surface wind speed; $sfcW_E$ represents near-surface wind speed from ERA5; $wind_G$ represents wind speed from the Global Wind Atlas; rlus represents surface upwelling longwave radiation; gsl represents growing season length; gsp represents growing season precipitation; gst represents growing season temperature; pet represents potential evapotranspiration; cmi represents the climate moisture index; awc represents available soil water capacity; swb represents site water balance. Green squares represent climate variables for which monthly time series are available for the period 1980–2018; orange squares represent variables for which future projections of climatologies exist; hashed squares represent variables with both time series for the recent past and future projections. Squares with border lines are part of the dataset presented.

– bioclimatic variables plus) dataset of global kilometer-resolution time series and climatologies for 15 climate-related variables. We compiled input data from CHELSA V.2.1 (Karger et al., 2021a) and other high-quality sources and used state-of-the-art approaches to generate two groups of biologically relevant climate-related variables: for one group of variables, we created time series covering 39 years of the recent past (hereafter: time-series variables), and for the other group we created climatologies for current and expected future conditions (hereafter: projected variables). Time-series variables are available for the period of 1980–2018 and include near-surface relative humidity (hurs), cloud area fraction (clt), near-surface wind speed (sfcWind), vapor pressure deficit (vpd), surface downwelling shortwave radiation (rsds), pet, and cmi, each containing 468 monthly layers at a 30 arcsec resolution (i.e., less than 1 km), and an annual statistic, i.e., site water balance (swb), containing 38 annual layers. For all of these variables but site water balance, we further calculated climatologies monthly, annually, and for annual ranges and extrema for the period 1981–2010, which is the climate-normal period recommended by the World Meteorological Organization (Arguez and Vose, 2011). Projected variables include frost change frequency (fcf), snow cover days (scd), potential net primary productivity (npp), growing degree days (gdd), growing season length (gsl), growing season temperature (gst), and growing season precipitation (gsp), for which we calculated climatological means for the same kilometer-resolution grid for the periods 1981–2010, 2011–2040, 2041–2070, and 2071–2100. For the latter three periods, climatological values were generated for each combination of three shared socioeconomic pathways (SSPs, O'Neill et al., 2014) and five Earth system models. To demonstrate the robustness of these variables, we validated them, where feasible, against global sets of observations from meteorological stations, and we compared them with existing products. Together, our layers of climate-

related variables allow the characterization of each pixel of the life-supporting landmass on Earth far more comprehensively than would be possible from temperature and precipitation alone: for the recent decades with monthly resolution and until the end of this century as projected climatologies.

2 Material and methods

We developed 15 climate-related variables that complement and build on existing products of the CHELSA initiative (Karger et al., 2017). We classified these variables into five orders, representing increasing degrees of abstraction from in situ measurements (Fig. 1). First-order variables are directly measurable properties, including near-surface temperature (daily means and extrema), precipitation rates, near-surface relative humidity, cloud area fraction, solar radiation, and near-surface wind speed. While downscaled climatologies and time series of temperature and precipitation rates have been made available previously (Karger et al., 2017, 2020, 2021b), here we downscaled corresponding layers for the remaining first-order variables clt, near-surface (10 m), and hurs. Directly based on these first-order variables, we have generated time series and climatologies for five biologically meaningful second-order variables, including fcf, scd, potential npp, and vpd. In addition, we aggregated daily high-resolution time series of rsds that have been developed in a related study (Karger et al., 2022). Similarly, we have generated time series and climatologies of four third-order climate variables (based on first- and second-order variables), including gsl, gsp, and gst, and pet as well as one fourth- and one fifth-order variable, i.e., the cmi and the swb, respectively.

2.1 Input data

Data on near-surface air temperature (tasmin, tasmax, tas) as well as precipitation rates (pr) and rsds have been taken from CHELSA V2.1 (Karger et al., 2021b). For past conditions, forcing from ERA5 (Hersbach et al., 2020) with a GPCC bias correction (Ziese et al., 2018) was used as well as an air temperature algorithm that builds on an atmospheric lapse rate-based downscaling (Karger et al., 2017). Precipitation rates are based on a mechanistic downscaling that takes orographic effects into account (Karger et al., 2021b). rsds in CHELSA V2.1 is based on a terrain-specific, mechanistic model (Böhner and Antonic, 2009). For tasmin, tasmax, tas, and pr we also used data on projected monthly climatologies for the periods 2011–2040, 2041–2070, and 2071–2100 from CHELSA V2.1. Such climatologies were generated for three official SSPs (O'Neill et al., 2016, 2017): SSP126 is an optimistic emission scenario, assuming that the world shifts gradually to a more sustainable path, resulting in an additional radiative forcing of 2.6 W m^{-2} by 2100 relative to preindustrial levels, SSP370 is an intermediate-to-pessimistic scenario, assuming that international fragmentation and regional rivalry hamper efficient implementations of globally sustainable solutions, leading to an additional radiative forcing of 7.0 W m^{-2} by 2100, and SSP585 is a pessimistic emission scenario, assuming that developing countries follow the trajectories of first-world countries in rapid economic development that hardly relies on greenhouse-gas-efficient technologies. It assumes an additional radiative forcing of 8.5 W m^{-2} by 2100. For each of these SSPs, we used global simulations of five Earth system models that were prepared for the Intersectoral Impact Model Intercomparison Project round 3b (ISIMIP3b, https://www.isimip.org/, last access: 21 January 2020) to generate future climatic anomalies of precipitation and temperature. Earth system models were chosen based on the availability of all needed climate variables and model performances following ISIMIP3b (Lange, 2021) and included GFDL-ESM4 (Held et al., 2019), IPSL-CM6A-LR (Boucher et al., 2020), MPI-ESM 1-2-HR (Gutjahr et al., 2019), MRI-ESM2-0 (Yukimoto et al., 2019), and UKESM1-0-LL (Sellar et al., 2019). In a first step, for each variable (tasmin, tasmax, tas, and pr), the dynamic model outputs were used to generate monthly climatologies for the 3 periods $\times 3$ SSPs $\times 5$ Earth system models. In addition, for each Earth system model and climate variable, one climatology was generated for the period 1981–2010. Then, each of these climatologies was downscaled to 30 arcsec using the delta-change method (Hay et al., 2000).

In addition, we compiled data for orography (orog), wind speed (wind$_G$, sfcW$_E$), relative humidity (hur), total cloud cover (tcc), surface upwelling longwave radiation (rlus), and available soil water content (awc). Orography data originated from the Global Multi-resolution Terrain Elevation Data 2010 (GMTED2010; Danielson and Gesch, 2011) at a resolution of 30 arcsec. We obtained two types of wind speed data: long-term averages at high spatial resolution (9 arcsec) and monthly time series at coarser spatial resolution. Wind speed averages for the period 2008–2017 at 10 (wind$_{G_{10}}$) and 50 (wind$_{G_{10}}$) m above the surface were obtained from the Global Wind Atlas 3.0, a free, web-based application developed, owned, and operated by the Technical University of Denmark (https://globalwindatlas.info, last access: 28 July 2021). From these layers, we derived roughness length as

$$z_0 = e^{\frac{\text{wind}_{G_{10}} \ln(50) - \text{wind}_{G_{50}} \ln(10)}{\text{wind}_{G_{10}} - \text{wind}_{G_{50}}}}. \quad (1)$$

Then, we aggregated wind$_{G_{10}}$ and roughness length from the original 9 arcsec resolution to 30 arcsec, using a two-step approach. First, we aggregated to 27 arcsec (factor of 3) by the median, and then we resampled to 30 arcsec, using cell area-weighted means. Finally, in order to keep aggregated roughness length estimates in a realistic range and to remove a few outliers, we bounded them by the typical values for the open sea (0.0002) as minimum and city centers with skyscrapers/-mountain tops (4) as maximum (WMO, 2018). Monthly time series of wind speed 10 m above the surface were obtained from the ERA5 global reanalysis product (sfcW$_E$, Hersbach et al., 2020) released by the European Centre for Medium-

Table 1. Input data used to generate the CHELSA-BIOCLIM+ dataset.

Variable name	Description	Spatial resolution	Temporal resolution	Time period	Source
tasmin	Daily minimum near-surface air temperature	30 arcsec	Monthly	1979–2019	Karger et al. (2017)
		0.5°		2011–2100	ISIMIP3b
tasmax	Daily maximum near-surface air temperature	30 arcsec	Monthly	1979–2019	Karger et al. (2017)
		0.5°		2011–2100	ISIMIP3b
tas	Mean near-surface air temperature	30 arcsec	Monthly	1979–2019	Karger et al. (2017)
		0.5°		2011–2100	ISIMIP3b
pr	Precipitation rate	30 arcsec	Monthly	1979–2018	Karger et al. (2017)
		0.5°		2011–2100	ISIMIP3b
rsds	Surface downwelling shortwave radiation	30 arcsec	Daily	1980–2018	Karger et al. (2022)
orog	Orography	30 arcsec	–	–	Danielson and Gesch (2011)
hur	Relative humidity	0.25°	Monthly	1980–2018	ERA5
tcc	Total cloud cover	0.25°	Monthly	1980–2018	ERA5
sfcWE	Wind speed at 10 m above the surface	0.25°	Monthly	1979–2020	ERA5
rlus	Surface upwelling longwave radiation	0.1°	Monthly	1979–2020	ERA5-Land
$\text{wind}_{G_{10}}$	Wind speed at 10 m above the surface	9 arcsec	–	2008–2017	Global Wind Atlas 3.0
$\text{wind}_{G_{50}}$	Wind speed at 50 m above the surface	9 arcsec	–	2008–2017	Global Wind Atlas 3.0
awc	Available soil water capacity	30 arcsec	–	–	SoilGrids

Range Weather Forecasts (ECMWF) and covered the period 1979–2020 with a horizontal resolution of 0.25°. From ERA5, we also used hur and tcc at 0.25° resolution monthly for the period 1980–2018. Monthly information on the surface upwelling longwave radiation needed for the calculation of pet was obtained from the ERA5-Land reanalysis product (Muñoz Sabater, 2019, 2021) that is also maintained by the ECMWF. It covered the period 1979–2020 with a horizontal resolution of 0.1°. Information on awc was obtained from SoilGrids (Hengl et al., 2014, 2017) with a horizontal resolution of 30 arcsec and a vertical resolution of six soil layers. From these data, we calculated one layer of available water volume by integrating over the soil profiles. A summary of all input data used is provided in Table 1.

2.2 Generating raster layers

2.2.1 First-order climate layers

Near-surface relative humidity

Near-surface relative humidity controls the biologically important variable vapor pressure deficit (see below) as well as fog formation (at hurs = 100 %), which can be a critical water source for vegetation in certain coastal ecosystems (e.g., in the California redwood forest; Dawson, 1998). We calculated hurs from atmospheric hur at pressure levels z. We used all pressure levels from ERA5 and horizontally B-spline (S_{xy})-interpolated hur at pressure levels $z_{i=1} \ldots z_{\text{n}}$ to a 30 arcsec resolution, using longitude (x) and latitude (y) as predictors and hur as a response, so that

$$S_{\text{xy}}(\text{hur}) = f(x, y). \tag{2}$$

From the resulting spline-interpolated values S_{xy} (hur) for each pressure level z, we then calculated a vertical spline interpolation separately for each 30 arcsec grid cell, using the geopotential height of each layer divided by the gravitational constant $g = 9.80665\,\text{m}\,\text{s}^{-2}$ as a predictor and the values given by the function S_{xy} (hur) as a response so that

$$S_z(\text{hur}) = S\left(S_{\text{xy}}(\text{hur})\right) = f(z). \tag{3}$$

We then used the vertical spline S_z (hur) to calculate a first approximation of $\text{hurs}_{\text{orog}}$ at 30 arcsec, with orog referring to surface elevation. This first approximation of the relative humidity at the surface, however, does not include orographic effects such as increased hurs on the windward sides and lower hurs on the leeward sides of an orographic barrier. Moist air is rising on the windward side of an orographic

barrier, potentially losing moisture and cooling with a wet-adiabatic lapse rate, and sinking on its leeward side, usually warming with a higher, dry-adiabatic lapse rate. This effect of differing adiabatic lapse rates and consequent temperature changes affects relative humidity. To include these orographic effects in the estimation of hurs, we use

$$\text{hurs} = \frac{1}{(1+\exp(-1\cdot h))}, \tag{4}$$

with

$$h = \frac{h_\text{t}\cdot(H+(H_c-H)(1-H_c))}{H_c} \tag{5}$$

and h_t being the logit-transformed version of hurs_orog:

$$h_\text{t} = \log\left(\frac{\text{hurs}_\text{orog}}{1-\text{hurs}_\text{orog}}\right), \tag{6}$$

H being the windward leeward index at 30 arcsec resolution calculated following the same parametrization as used in Karger et al. (2021b) and H_c being the spline-interpolated mean of all H values that overlap with the respective 0.25° grid cell from ERA5. We calculated hurs monthly for the period 1980–2018. For the period 1981–2010, we derived monthly climatologies and climatological means, annual ranges, and extrema. All hurs data are reported as percentages.

Cloud area fraction

The cloud area fraction represents the fraction of a grid cell that is covered by clouds across the entire atmospheric column, as seen from the Earth's surface or the top of the atmosphere. It includes both large-scale and convective clouds. Cloud area fraction determines the amount of downwelling solar radiation that reaches the Earth's surface and is an important constraint on productivity in tropical ecosystems (Nemani et al., 2003). Moreover, low-hanging clouds can be a key water source, and thus in mountain regions clt can be an important determinant of the distribution of tropical cloud forests (Karger et al., 2021c). We calculated clt monthly for the period 1980–2018 based on tcc and following the procedure described in Karger et al. (2022). Unlike all other variables presented here, we downscaled clt to a cruder spatial resolution of 1.5 arcmin. This resolution was chosen because it is similar to the resolution at which orographic wind effects for precipitation are calculated (Karger et al., 2021b) and because it avoids over-representing terrain effects (Daly et al., 1997). For the period 1981–2010, we derived monthly climatologies and climatological means, annual ranges, and extrema. All clt data are reported as percentages.

Near-surface wind speed

Numerous direct and indirect effects of wind speed on terrestrial ecosystems exist, including gas and heat exchange, dispersal of pollen, seeds, pests or pollutants, and wind throw (Nobel, 1981). The impacts of wind exposure on microclimate and vegetation patterns are particularly evident, for example, in the polar and subpolar zones (Schultz, 2005). We estimated monthly averages of sfcWind at 30 arcsec resolution by downscaling and bias-correcting the ERA5 time series (sfcW_E) using an aggregation of the Global Wind Atlas product ($\text{wind}_{G_{10}}$; see subsection "Input data"). In a first step, we averaged sfcW_E for the period 2008–2017, for which the Global Wind Atlas is representative. Then, we estimated the average deviation between sfcW_E and $\text{wind}_{G_{10}}$. This deviation raster contained information about both small-scale deviations from the ERA5 cell mean due to topography and bias in long-term estimates of wind speed. Next, we added this difference layer to each monthly ERA5 layer (from 1979 to 2019) after log-transforming all layers. Our approach therefore corresponded to the delta-change method (Hay et al., 2000), except that we applied it to log-transformed wind speed estimates. This was done because wind speed follows a Weibull distribution (Weibull, 1951), which can be related to the normal distribution through a log-link function. Finally, we back-transformed the two-layer sums by exponentiating them. For the period 1981–2010, we derived monthly climatologies of sfcWind and climatological means, annual ranges, and extrema. All sfcWind data are reported in meters per second.

2.2.2 Second-order climate layers

Frost change frequency

Frost change frequency describes the number of days per year with temperature minima below 0 °C and maxima above 0 °C. Coping with frost requires adapted behaviors or elaborate physiological adaptations for both ectothermal and endothermal organisms and especially for non-migrating life forms that cannot escape, such as plants. Frost change frequency carries information about the occurrence frequency of freezing and thawing events and – indirectly – about their duration, both of which are crucial constraints determining the best-suited adaptation strategies; see, e.g., Hufkens et al. (2012). We used a B-spline interpolation S (tasmax, t) and S (tasmin, t) to get both daily minimum (tasmin_i) and maximum (tasmax_i) near-surface 2 m air temperatures from monthly values, with t the sequence of Julian days marking the middle of each month, i.e., [349, 15, 45, 74, 105, 135, 166, 196, 227, 258, 288, 319, 349, 15]. As B-spline interpolations cannot predict values outside their bounding knots, we first extended the sequence of knots to start on 15 December (Julian day 349) and end on 15 January (Julian day 15) and cut the interpolated sequence to range from 1 January to 31 December in a second step. A frost change event was then defined by $\text{tasmin}_i < 0$ °C and $\text{tasmax}_i > 0$ °C. We calculated fcf from the monthly climatologies of tasmin and tasmax for the periods 1981–2010, 2011–2040, 2041–2070, and 2071–2100 for all combinations of SSPs and Earth system models

(see subsection "Input data"). fcf is reported as the number of days per year with frost change events.

Snow cover days

Snow cover days are the number of days per year on which the ground is covered with snow. Snow cover affects local climate, hydrology, and ecosystems in complex ways (Callaghan et al., 2011; Schultz, 2005) by insulating the soil from temperature minima during winter months (Zhang, 2005), determining Arctic vegetation patterns (Evans et al., 1989), or providing hiding opportunities from predators for small mammals (Callaghan et al., 2011). We used a B-spline interpolation S (tas, t) to get from monthly to daily estimates of tas, with t being a vector of Julian days marking the middle of each month, i.e., [349, 15, 45, 74, 105, 135, 166, 196, 227, 258, 288, 319, 349, 15], and tas being the mean of near-surface 2 m air temperature for the respective month. We used a stepwise interpolation of monthly precipitation rates to daily precipitation rates following Paulsen and Körner (2014). The daily pr in this approach is directly coupled to the near-surface air temperature as follows.

$$\mathrm{pr} = \begin{cases} 5\,\mathrm{kg}\cdot\mathrm{m}^{-2}\cdot\mathrm{d}^{-1} & \text{if tas} < 5\,^{\circ}\mathrm{C} \\ 10\,\mathrm{kg}\cdot\mathrm{m}^{-2}\cdot\mathrm{d}^{-1} & \text{if } 5\,^{\circ}\mathrm{C} \le \text{tas} < 10\,^{\circ}\mathrm{C} \\ 15\,\mathrm{kg}\cdot\mathrm{m}^{-2}\cdot\mathrm{d}^{-1} & \text{if } 10\,^{\circ}\mathrm{C} \le \text{tas} < 15\,^{\circ}\mathrm{C} \\ 20\,\mathrm{kg}\cdot\mathrm{m}^{-2}\cdot\mathrm{d}^{-1} & \text{if } 15\,^{\circ}\mathrm{C} \le \text{tas} \end{cases} \quad (7)$$

The total amount of pr is distributed to as many rainfall events as are necessary to obtain the monthly amount of precipitation, with events being evenly distributed across the month. Precipitation is solid (snow) when tas$<0\,^{\circ}$C and accumulates as long as tas remains below $0\,^{\circ}$C. If tas$>0\,^{\circ}$C, it melts by a rate of $0.84\,\mathrm{kg\,m^{-2}\,d^{-1}\,K^{-1}}$ (Paulsen and Körner, 2014). When liquid precipitation falls on an existing snow layer, it cools to $0\,^{\circ}$C, and the thermal energy released ($4.186\,\mathrm{kJ\,kg^{-1}\,K^{-1}}$) is assumed to melt snow (Körner et al., 2011). The number of snow cover days is then given by the days of the year on which a snow layer with a snow water content of $\geq 1\,\mathrm{kg\,m^{-2}}$ existed. We calculated scd from the monthly climatologies of tas and pr for the periods 1981–2010, 2011–2040, 2041–2070, and 2071–2100 for all combinations of SSPs and Earth system models (see subsection "Input data"). scd is reported as the number of days per year with snow cover.

Potential net primary productivity

Potential net primary productivity is the potential difference between the rate at which carbon is fixed by photoautotrophs and the rate at which carbon is emitted through cell respiration if only climate was limiting. Primary productivity is the main way in which carbon dioxide is removed from the atmosphere and biomass is produced and is thus a key ecosystem function (Schimel, 1995). Here, we used the Miami model (Lieth, 1975) to estimate npp solely based on climatic constraints, resulting in a potential estimate that is independent of the existing vegetation on the ground. The unit of npp is $\mathrm{g\,m^{-2}\,yr^{-1}}$, where "g" stands for grams of dry matter. The estimates are based on mean annual near-surface 2 m air temperature in $^{\circ}$C and annual precipitation rates in $\mathrm{kg\,m^{-2}\,yr^{-1}}$. The Miami model assumes that npp increases asymptotically with both increasing temperature and increasing precipitation, approaching an upper limit of $3000\,\mathrm{g\,m^{-2}\,yr^{-1}}$. The precipitation component of npp is given as

$$\mathrm{npp_{pr}} = 3000 \times (1 - \exp(-0.000664 \times \mathrm{pr})), \quad (8)$$

and the air temperature component is given as

$$\mathrm{npp_{tas}} = 3000 \times (1 + \exp(1.315 - 0.119 \times \mathrm{tas}))^{-1}. \quad (9)$$

Based on these two components, npp is either limited by temperature or precipitation and determined by the minimum estimate of npp from either the temperature or the precipitation component:

$$\mathrm{npp} = \min\left(\mathrm{npp_{tas}}, \mathrm{npp_{pr}}\right). \quad (10)$$

We calculated npp from the monthly climatologies of tas and pr for the periods 1981–2010, 2011–2040, 2041–2070, and 2071–2100 for all combinations of SSPs and Earth system models (see subsection "Input data").

Growing degree days

Growing degree days are a measure of heat accumulation over a specific time period. They have been used to understand the phenology of plants and animals for centuries in agronomy (Anandhi, 2016) and for a shorter period in ecology (Cayton et al., 2015). It has been shown that the heat sum above a critical threshold accumulated through time better explains, e.g., plant phenology than a threshold temperature alone (Larcher, 1994). The gdd threshold temperature ascertains that cool periods, during which phenological progress stagnates, are omitted. The threshold temperature is species-specific and varies, e.g., between $0\,^{\circ}$C for cold-adapted plants (Larcher, 1994) and 5 or $5.5\,^{\circ}$C for many temperate to boreal tree species (Prentice et al., 1992; Lenihan, 1993), while tropical plants are limited by temperatures below $10\,^{\circ}$C and even much higher (Larcher, 1994). Growing degree days are calculated by first assessing whether daily mean near-surface 2 m air temperatures surpass a baseline threshold temperature $\mathrm{tas_b}$ (e.g., $5\,^{\circ}$C) and then summing all the surpluses. To obtain daily estimates of near-surface 2 m air temperature from monthly values, we have used the same approach of B-spline interpolation as for snow cover days. The growing degree sum is then given as the sum

$$\mathrm{gdd_b} = \sum_{i=1}^{365} (\max(\mathrm{tas}_i - \mathrm{tas_b}, 0)), \quad (11)$$

where tas_b is the baseline temperature and i represents the Julian day. We calculated gdd for three baseline temperatures (0, 5, and 10 °C) from the monthly climatologies of tas for the periods 1981–2010, 2011–2040, 2041–2070, and 2071–2100 for all combinations of SSPs and Earth system models (see subsection "Input data"). However, here we only report the results for gdd with the 5 °C baseline (gdd_5). All gdd data are reported as degree days (°C d).

Vapor pressure deficit

Vapor pressure deficit is the difference between the actual amount of moisture in the air and the maximum amount of moisture the air can hold at a given temperature. vpd is a key meteorological property for terrestrial biomes, determining plant functioning and drought-induced mortality (Grossiord et al., 2020). Moreover, the distributions of animals prone to desiccation such as small arthropods are limited by vpd (Hauser et al., 2018; Ouisse et al., 2016). Near-surface vpd can be calculated from hurs, considered a unitless fraction, and tas in °C as

$$\mathrm{vpd} = e_{\mathrm{sat}}(\mathrm{tas}) \times (1 - \mathrm{hurs}), \tag{12}$$

where $e_{\mathrm{sat}}(\mathrm{tas})$ is the saturation vapor pressure. In order to approximate $e_{\mathrm{sat}}(\mathrm{tas})$, we used the Magnus equation with the coefficients of Sonntag (1990):

$$e_{\mathrm{sat}}(\mathrm{tas}) = 0.6112 \times e^{\frac{17.62 \cdot \mathrm{tas}}{(243.12 + \mathrm{tas})}}. \tag{13}$$

vpd was calculated in the R environment (R Development Core Team, 2008), using the package bigleaf (Knauer et al., 2018). We calculated vapor pressure deficit monthly for the period 1980–2018. For the period 1981–2010, we derived monthly climatologies and climatological means, annual ranges, and extrema. All vpd data are reported in Pascal (Pa).

Surface downwelling shortwave radiation

rsds is the amount of direct and diffuse shortwave radiation that reaches the Earth's surface, considering the filtering effects of air and clouds throughout the atmosphere as well as the effects of the local topography. rsds describes the amount of solar energy available. It can critically affect local climate and vegetation patterns in high-latitude environments (Andrade et al., 2018; Schultz, 2005). In the tropics with year-round rain, where temperature and precipitation are not limiting, it can constrain primary productivity (Nemani et al., 2003). To calculate rsds, surface downwelling solar radiation under clear-sky conditions (rsdscs) is first calculated by computing 30 arcsec clear-sky radiation using the method described in Böhner and Antonic (2009) for each day of the year. Then daily estimates of rsdscs and clt are combined through the following relationship:

$$\mathrm{rsds} = \mathrm{rsdscs} \cdot \left(1 - 0.75 \cdot \mathrm{clt}^{3.4}\right). \tag{14}$$

In this way, daily estimates of rsds from 1980 to 2018 were generated in a related project (Karger et al., 2022). Here, we summarized these estimates to monthly means, and for the period 1981–2010 we derived monthly climatologies and climatological means, annual ranges, and extrema. All rsds data are reported in MJ m^{-2} d^{-1}.

2.2.3 Third-order climate layers

Growing-season-related predictors

The growing season is the annual period, during which conditions are favorable for vegetation growth. Growing season length indicates the amount of time available for plant growth, which is an important determinant of life-history traits and productivity (Paulsen and Körner, 2014). Like gdd, gsl is species-specific and can vary considerably between plants adapted to different biomes. Here, we estimate gsl for tree species forming treelines, i.e., growing at the cold/dry boundary of forested biomes worldwide. Under such conditions gsl can be defined as the number of days per year with temperatures >0.9 °C, with no snow cover being present and with sufficient water available in the soil (Paulsen and Körner, 2014). Daily precipitation rates and near-surface 2 m air temperature averages were calculated in the same way as for snow cover. In addition, potential evapotranspiration was estimated using the Hargreaves equation and tasmin and tasmax as input (Hargreaves and Samani, 1985). Note that this estimate of pet is specific to the estimated growing season-related predictors and is independent of the more sophisticated approach presented below. Water balance in the soil was calculated by a two-layer bucket model. The upper layer is assumed to be able to hold 30 kg of liquid water per square meter at maximum. For the lower layer we used empirical data on water holding capacity awc (see "Input data"). Liquid precipitation or snowmelt fills the upper layer first. If the soil water content of the upper layer (swc_1) exceeds 30 kg m^{-2}, water flows to the lower layer until saturated. If the second layer is saturated, the remaining flux is assumed to be lost as runoff. If water is present in the upper layer, actual evapotranspiration (aet) is equal to pet. We used a square-root correction for the estimation of the actual daily evapotranspiration from deeper layers as soon as the upper layer was empty: $\mathrm{aet} = \mathrm{pet} \times (\mathrm{swc}_2/\mathrm{awc})^{1/2}$ in kg m^{-2} d^{-1}, with soil water given in kg m^{-2}. A growing season day is defined as a day on which $swc_1 > 0$ and tas >0.9 °C and snow <1 kg m^{-2}. Growing season length is then the number of days per year on which this condition holds true, gsp is the amount of precipitation that falls during the days on which the condition is true, and gst is the mean near-surface air temperature during days on which the condition is true. We calculated gsl, gsp, and gst from the monthly climatologies of tasmin, tasmax, tas, and pr and from the scd estimates described above for the periods 1981–2010, 2011–2040, 2041–2070, and 2071–

2100 for all combinations of SSPs and Earth system models (see subsection "Input data").

Potential evapotranspiration

Potential evapotranspiration is defined as the amount of water per area and time that could evaporate at the soil surface or be transpired through plants if soil water availability was not limiting. Evapotranspiration is a crucial part of the water cycle and strongly interacts with vegetation traits such as leaf area (Irmak, 2008). We calculated pet with the Penman–Monteith equation (Monteith, 1965) as implemented in R package bigleaf (function "potential.ET"). This function builds on the following equation (Knauer et al., 2018):

$$\lambda E_{\text{pot}} = \frac{\Delta\,(R_{\text{n}} - G - S) + \rho \times c_p \times \text{vpd} \times \text{Ga}}{\Delta + \gamma\left(1 + \frac{\text{Ga}}{\text{Gs}_{\text{pot}}}\right)}, \quad (15)$$

where Δ is the slope of the saturation vapor pressure curve (kPa K^{-1}) that is approximated with Eq. (3), R_{n} is net radiation (W m^{-2}), G is the ground heat flux (W m^{-2}), S is the sum of all storage fluxes (W m^{-2}), ρ is the mean air density (kg m^{-3}), c_p is the specific heat of the air ($\text{J K}^{-1}\,\text{kg}^{-1}$), γ is the psychrometric constant (kPa K^{-1}), Ga is the aerodynamic conductance (m s^{-1}), and Gs_{pot} is the potential surface conductance ($\text{mol m}^{-2}\,\text{s}^{-1}$). To calculate pet with the bigleaf framework, information on the following general environmental conditions is required: tas, vpd, R_{n}, pressure, G, and S. For tas, we used monthly layers of the CHELSA tas product (see "Input data"). For vpd, we used the layers calculated here. R_{n} was calculated as the difference between rsds calculated here and rlus from ERA5-Land, following Singer et al. (2021). Since these radiation layers had different spatial resolutions (30 arcsec and 0.1°, respectively), we used the grid calculus tool of the System for Automated Geoscientific Analyses (SAGA, Conrad et al., 2015) to calculate the differences on the fine grid, using bilinear interpolation to downscale the coarse grid of rlus. In a few pixels (in rugged terrain) estimates of R_{n} could be negative, in which case we manually set them to zero. Pressure was calculated with the function "pressure.from.elevation" of R package bigleaf (Knauer et al., 2018), considering orography, tas, and vpd to be driving factors. Ground heat flux (G) was assumed to correspond to 10 % of R_{n} (Allen et al., 1998; Singer et al., 2021), and storage fluxes (S) were assumed to sum to zero.

In addition to general environmental conditions, information on aerodynamic and potential surface conductance was needed to calculate pet with the Penman–Monteith equation, and these metrics depend on the property of the surface considered. We estimated conductances for a reference crop of 12 cm height, using the simplified relationships provided by Allen et al. (1998). Ga was estimated as $\frac{w_{2*}}{208}$, with w_{2*} being wind speed 2 m above the roughness length (m s^{-1}). We derived w_{2*} from our monthly estimates of sfcWind (which are estimated 10 m above the surface) in the following way:

$$w_{2*} = \text{sfcWind} \times \frac{ln\left(\frac{z_0+2}{z_0}\right)}{\ln\left(\frac{10}{z_0}\right)}, \quad (16)$$

where z_0 is roughness length (see subsection "Input data"). Gs_{pot} was calculated assuming a constant surface resistance of $70\,\text{s m}^{-1}$ (Allen et al., 1998) and considering local tas and pressure (using the bigleaf function "ms.to.mol"). We calculated pet monthly from 1979 to 2019. For the period 1981–2010, we derived monthly climatologies of pet and climatological means, annual ranges, and extrema. All pet data are reported in $\text{kg m}^{-2}\,\text{month}^{-1}$.

2.2.4 Fourth-order climate layers

Climate moisture index

Climate moisture index is the difference between precipitation and potential evapotranspiration (Hogg, 1997). cmi informs about the moisture regime and has been related to biome boundaries and drought impact on tree health and regeneration (Hogg et al., 2017; Hogg, 1997). We calculated cmi for each month of the period 1980–2018 using the CHELSA pr layers and the pet layers generated in this study. For the period 1981–2010, we derived monthly climatologies of cmi and climatological means, annual ranges, and extrema. All cmi data are reported in $\text{kg m}^{-2}\,\text{month}^{-1}$.

2.2.5 Fifth-order climate layers

Site water balance

Site water balance is an estimate of the water available to plants during a year that considers soil parameters in addition to climate variables. swb has been shown to closely correlate with functional plant traits such as leaf area (Grier and Running, 1977; Gholz, 1982), and it is considered one of the main determinants of plant distribution (Neilson, 1995; Woodward, 1987). We used an approach similar to that of Grier and Running (1977) to calculate the site water balance. From the cmi climatologies, we identified the start of the hydrological year, i.e., either the first month after the arid period (with a negative cmi) or the month after the one with the lowest cmi. Then, monthly estimates of cmi are summed over the hydrological year, whereby the running sum is never allowed to exceed the available water volume of the soil (approximated here by awc; see "Input data"), and excess water is assumed to run off. When pet exceeds precipitation (negative cmi), the difference is subtracted from the water balance, which often leads to distinctly negative values over the course of a hydrological year. We calculated swb for each year of the period 1980–2018, i.e., choosing 1981 as the first representative year and allowing hydrological years to start in 1980 already. For the period 1981–2010, we derived climatological means. All swb data are reported in $\text{kg m}^{-2}\,\text{yr}^{-1}$.

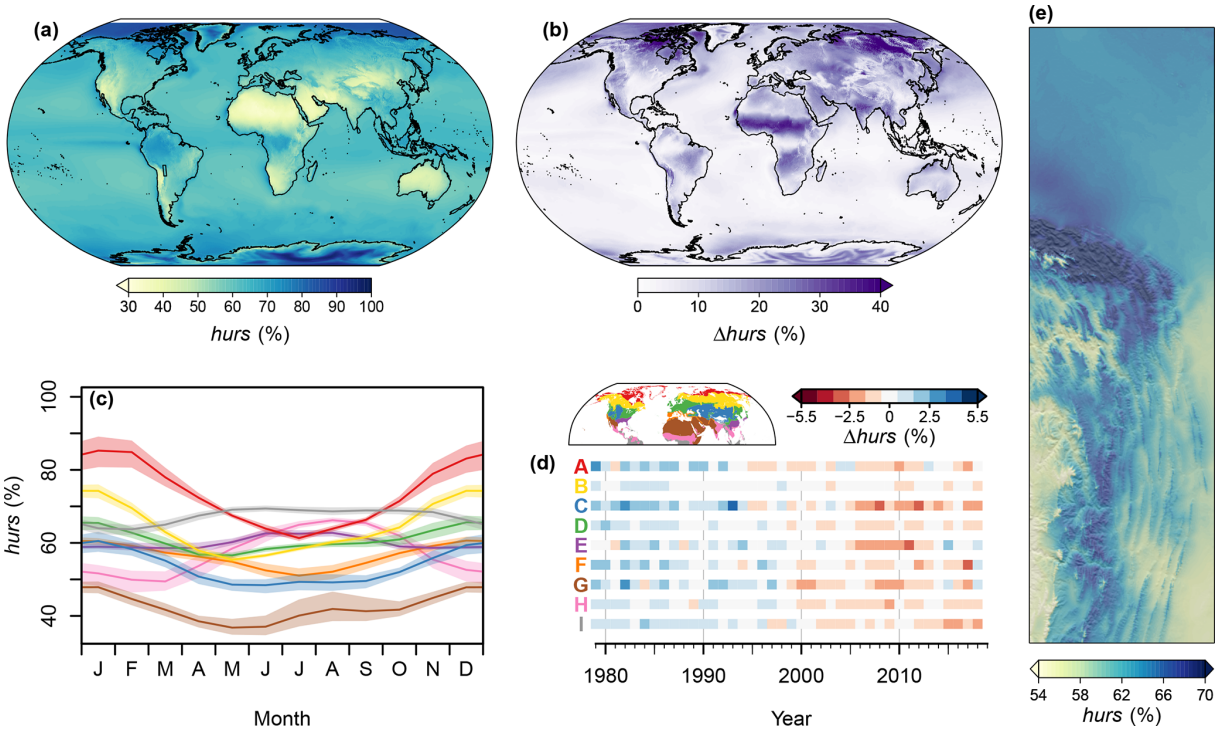

Figure 2. Overview of the spatiotemporal distribution of near-surface relative humidity (hurs). **(a)** Global map of the climatological mean for the period 1981–2010; **(b)** global map of the range (max–min) of monthly hurs means for the period 1981–2010; **(c)** seasonal cycle of hurs in the biomes of the Northern Hemisphere for the period 1981–2010. Polygons indicate the range from the 40th to 60th percentiles, and lines indicate medians. **(d)** Temporal change in annual mean hurs by biome. Shown are deviations in percent of the long-term (1979–2018) annual mean. Red (A) represents the polar and subpolar zone; yellow (B) represents the boreal zone; blue (C) represents dry midlatitudes; green (D) represents temperate midlatitudes; purple (E) represents subtropics with year-round rain; orange (F) represents subtropics with winter rain; brown (G) represents dry tropics and subtropics; pink (H) represents tropics with summer rain; grey (I) represents tropics with year-round rain. **(e)** An exemplary high-resolution map of the climatological mean of hurs for the northeastern boundary region of the Andes. For the exact location, see the inset in panel **(a)**.

2.3 Validation

2.3.1 Station data

We validated 9 of the 15 climate-related variables at three levels of temporal aggregation, using global sets of station measurements. We validated primarily variables that could either be measured directly or derived readily from measurements, using three different data sources. hurs, sfcWind, fcf, scd, gdd_5, and vpd were validated against station measurements from the Global Surface Summary of Day (GSOD) database (Global Surface Summary of Day, 2022), containing measurements of weather conditions of >28 000 stations globally, with a focus on the Northern Hemisphere. We used R package GSODR (Sparks et al., 2017) to download and quality-control daily averages from 1979 to 2020 and to calculate saturation vapor pressure, actual vapor pressure, and relative humidity from measured properties using the improved August–Roche–Magnus approximation (Alduchov and Eskridge, 1996). For each station, we then calculated vapor pressure deficit as the difference between saturation vapor pressure and actual vapor pressure, defined frost change days as days with maximum temperature >0 °C and minimum temperature <0 °C, defined daily growing degree days as average temperature minus 5 °C if the average temperature was >5 and 0 °C otherwise, and defined snow cover days as days with measured snow depth. To validate clt, we used station measurements from the HadISD (v.3.2.0.2021f) global subdaily database (Dunn, 2019) provided by the UK Met Office Hadley Centre (https://www.metoffice.gov.uk/hadobs/hadisd/ last access: 19 October 2022). For each station, we aggregated all 1979–2020 hourly, non-flagged measurements of total cloud cover to daily averages and converted the original eight-level scale to percent. Station measurements for pet and cmi were obtained from the World-wide Agroclimate Data of FAO (FAOCLIM; FAO, 2001). This agroclimatic database contains data for 28 800 stations and 14 observed and computed agroclimatic parameters. For validation, we used monthly climatologies provided by FAOCLIM version 2, which cover the period 1961–1990 and thus only partially overlap with our 1981–2010 climatologies. For potential evapotranspiration these values were available directly, while for the climate moisture index we calculated them

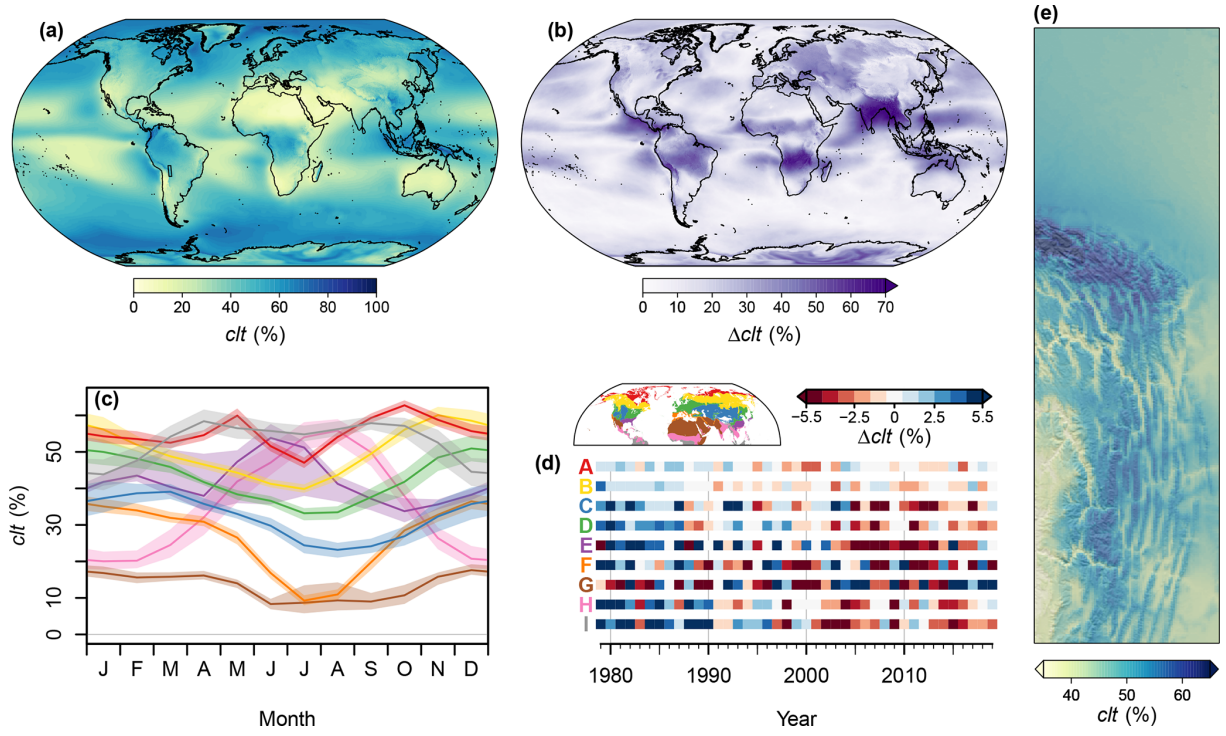

Figure 3. Overview of the spatiotemporal distribution of the cloud area fraction (clt). **(a)** Global map of the climatological mean for the period 1981–2010. **(b)** Global map of the range (max–min) of monthly clt means for the period 1981–2010. **(c)** Seasonal cycle of clt in the biomes of the Northern Hemisphere for the period 1981–2010. Polygons indicate the range from the 40th to 60th percentiles, and lines indicate medians. **(d)** Temporal change in annual mean clt by biome. Shown are deviations in percent of the long-term (1979–2019) annual mean. Red (A) represents the polar and subpolar zone; yellow (B) represents the boreal zone; blue (C) represents dry midlatitudes; green (D) represents temperate midlatitudes; purple (E) represents subtropics with year-round rain; orange (F) represents subtropics with winter rain; brown (G) represents dry tropics and subtropics; pink (H) represents tropics with summer rain; grey (I) represents the boundary region of the Andes. **(e)** An exemplary high-resolution map of the climatological mean of clt for the northeastern boundary region of the Andes. For the exact location, see the inset in panel **(a)**.

station-wise, considering only stations that simultaneously reported potential evapotranspiration and precipitation.

We aggregated station measurements temporally to three levels. Firstly, we aggregated data on hurs, clt, sfcWind, fcf, scd, gdd_5, and vpd by month. For hurs, clt, sfcWind, and vpd, we calculated monthly means for each combination of station and month for which 25 or more daily averages were available. For fcf, scd, and gdd_5, we calculated monthly sums when 25 or more daily estimates were available (for scd, we thereby considered temperature measurements, as snow depth was only reported when snow was present). If estimates were missing for some days, we multiplied the sum by the inverse of the fraction of days covered. Secondly, we aggregated hurs, clt, sfcWind, and vpd to monthly climatologies. To this end, we first filtered for measurements made between 1981 and 2010 and counted, for each combination of month and station, how many years were available. When data for more than 15 years existed, we calculated monthly climatological means. Finally, we calculated annual climatological means. For hurs, clt, sfcWind, vpd, pet, and cmi, we did this by station-wise averaging monthly climatologies, considering stations for which estimates were missing for no more than 1 month. For fcf, scd, and gdd_5, we first derived yearly sums from 1981 to 2010, expecting 12 monthly sums per station and year. For scd we did this for all combinations of stations and years with at least one observation of snow depth per year, and we further considered combinations of stations and years with daily temperature minima consistently above °C as having zero snow cover days. Then, we calculated climatological means for stations with more than 15 yearly sums.

2.3.2 Gridded data

In addition to station measurements, we compared CHELSA-BIOCLIM+ variables to gridded data from station-based interpolation and from a weather research and forecasting (WRF) model simulation. Gridded data from station-based interpolations originated or were built from WorldClim v2.0 (Fick and Hijmans, 2017) and from the Global Aridity Index and Potential Evapotranspiration Database version 3 (Zomer et al., 2022) and had a global

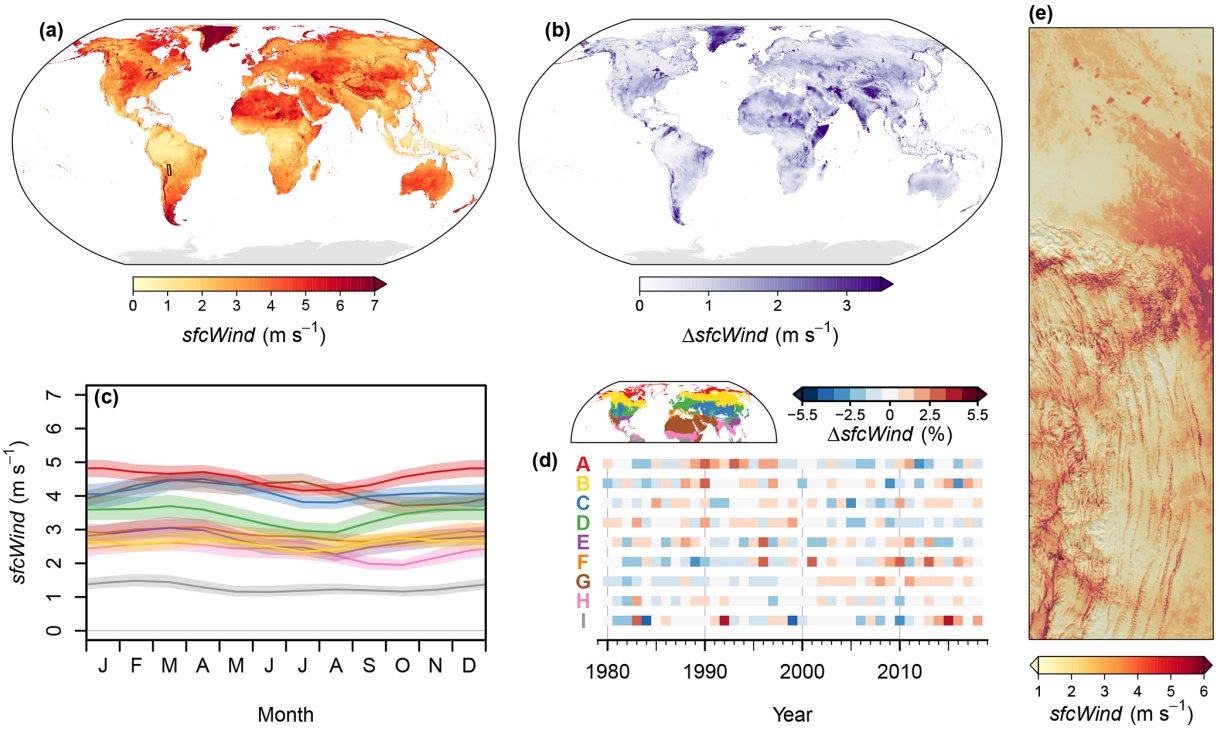

Figure 4. Overview of the spatiotemporal distribution of near-surface wind speed (sfcWind). **(a)** Global map of the climatological mean for the period 1981–2010. **(b)** Global map of the range (max–min) of monthly sfcWind means for the period 1981–2010. **(c)** Seasonal cycle of sfcWind in the biomes of the Northern Hemisphere for the period 1981–2010. Polygons indicate the range from the 40th to 60th percentiles, and lines indicate medians. **(d)** Temporal change in long-term (1980–2018) annual mean sfcWind by biome. Shown are deviations in percent of the annual mean. Red (A) represents the polar and subpolar zone; yellow (B) represents the boreal zone; blue (C) represents dry midlatitudes; green (D) represents temperate midlatitudes; purple (E) represents subtropics with year-round rain; orange (F) represents subtropics with winter rain; brown (G) represents dry tropics and subtropics; pink (H) represents tropics with summer rain; grey (I) represents tropics with year-round rain. **(e)** An exemplary high-resolution map of the climatological mean of sfcWind for the northeastern boundary region of the Andes. For the exact location, see the inset in panel **(a)**.

coverage and spatial resolution of 30 arcsec. We calculated annual climatologies from WorldClim's monthly wind speed and solar-radiation climatologies and from the monthly climatology of Global-AI_PET's potential evapotranspiration. Moreover, we derived estimates for relative humidity, vapor pressure deficit, and climate moisture index. We calculated relative humidity and vapor pressure using WorldClim's vapor pressure, maximum temperature, and minimum temperature following the procedure described in Zomer et al. (2022). For the climate moisture index, we subtracted Global-AI_PET's potential evapotranspiration from WorldClim's precipitation. Derived variables were first calculated for each climatological month and then averaged to annual climatologies. Note that these climatologies are representative for the period 1970–2000 and thus only partially overlap with the CHELSA-BIOCLIM+ climatologies.

For a second comparison, we considered outputs of the High Asia Refined analysis version 1 (Maussion et al., 2011, 2014) that were generated through dynamical downscaling using WRF model version 3.3.1 (Skamarock and Klemp, 2008). Simulated layers have a resolution of 10 km and are representative of the period 2000–2014, which only partially overlaps with the CHELSA-BIOCLIM+ climatologies. From these simulations, we used wind speed 10 m above the surface and downward shortwave flux at the ground surface (compared to rsds) after converting the units. Relative humidity and vapor pressure deficit were derived from daily estimates of water vapor mixing ratio (q), temperature at 2 m (tas), and surface pressure (p). To this end, we first calculated saturation vapor pressure from temperature, using Eq. (13), and actual vapor pressure according to the formula

$$e_a = \frac{q \cdot p}{q \cdot (1 - \mathrm{MW_{ratio}}) + \mathrm{MW_{ratio}}}, \tag{17}$$

where $\mathrm{MW_{ratio}}$ is the ratio of molecular weights of water vapor and dry air and equals 0.622. Relative humidity was then calculated by dividing actual vapor pressure by saturation vapor pressure, and vapor pressure deficit was calculated as the difference between saturation vapor pressure and actual vapor pressure. Daily estimates of relative humidity and vapor pressure deficit were aggregated to 2000–2014 averages.

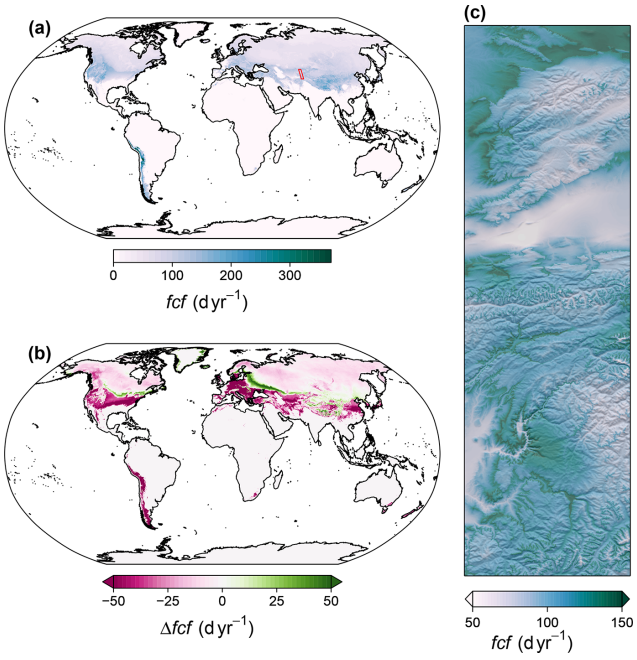

Figure 5. Overview of the spatiotemporal distribution of frost change frequency (fcf): **(a)** global map of the climatological mean of fcf for the period 1981–2010; **(b)** global map of the difference between climatological means of 2071–2100 and 1981–2010, assuming anthropogenic emissions to follow the shared socioeconomic pathway SSP370 and building on projections of the Max Planck Institute Earth System Model (MPI-ESM 1-2-HR); **(c)** an exemplary high-resolution map of the climatological mean for the western edge of the Himalayas. For the exact location, see the inset in panel **(a)**.

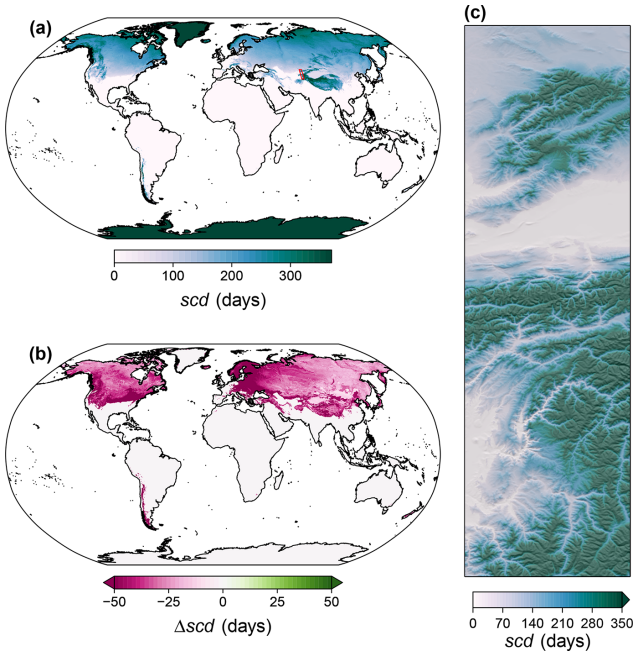

Figure 6. Overview of the spatiotemporal distribution of snow cover days (scd): **(a)** global map of the climatological mean of scd for the period 1981–2010; **(b)** global map of the difference between climatological means of 2071–2100 and 1981–2010, assuming anthropogenic emissions to follow the shared socioeconomic pathway SSP370 and building on projections of the MPI-ESM 1-2-HR. **(c)** An exemplary high-resolution map of the climatological mean for the western edge of the Himalayas. For the exact location, see the inset in panel **(a)**.

Potential evaporation was converted from Watts per square meter to kilograms per square meter per year using a linear approximation of the temperature dependency of the energy needed to vaporize water (ΔHvap in J kg^{-1}):

$$\Delta\text{Hvap} = 3.148 \times 10^6 - 2370 \times \text{tas}, \quad (18)$$

whereby the 2000–2014 averages of potential evaporation and tas were used. Finally, climate moisture index was calculated as the difference between potential evaporation and precipitation.

2.3.3 Summary statistics and visualizations

We matched station measurements with CHELSA-BIOCLIM+ layers and station-based interpolations at the different levels of temporal aggregation and calculated summary statistics. For the various combinations of variable, origin (CHELSA-BIOCLIM+ or station-based interpolation), and temporal aggregation (monthly, monthly climatology, and annual climatology), we matched station-based measurements with gridded data, and we converted variables to the same units as the CHELSA-BIOCLIM+ layers. Then, we derived the number of stations for which both measurements and corresponding gridded data existed and calculated Pearson correlation coefficients (r), mean absolute error (MAE), root mean squared error (RMSE), absolute bias, as well as the average across station measurements. Moreover, for annual climatologies we plotted MAE in space, and we calculated and visualized r for each time step for validated time-series variables (hurs, clt, sfcWind, and vpd) and for validated monthly climatologies (hurs, clt, sfcWind, vpd, pet, and cmi).

In addition to these validation results, we present detailed visualizations of spatial and temporal patterns for each variable. We show global maps as well as fine-scale patterns for one of two selected regions. For time-series variables, we report seasonal and long-term variations for different biomes, as defined by Schultz (2005), and for projected variables we show differences between the climatological means for 1981–2010 and 2071–2100, assuming an SSP370 pathway and considering the MPI-ESM 1-2-HR model. Finally, for the Himalayan region, we visually compare the fine-scale patterns for hurs, sfcWind, rsds, vpd, pet, and cmi between CHELSA-BIOCLIM+, station-based interpolations, and WRF outputs.

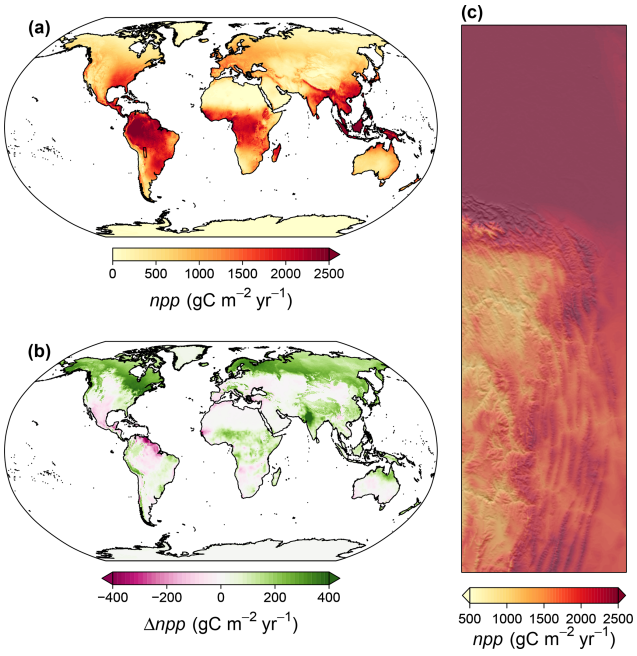

Figure 7. Overview of the spatiotemporal distribution of net primary productivity (npp). **(a)** Global map of the climatological mean of npp for the period 1981–2010. **(b)** Global map of the difference between climatological means of 2071–2100 and 1981–2010, assuming anthropogenic emissions to follow the shared socioeconomic pathway SSP370 and building on projections of the MPI-ESM 1-2-HR. **(c)** An exemplary high-resolution map of the climatological mean for the northeastern boundary region of the Andes. For the exact location, see the inset in panel **(a)**.

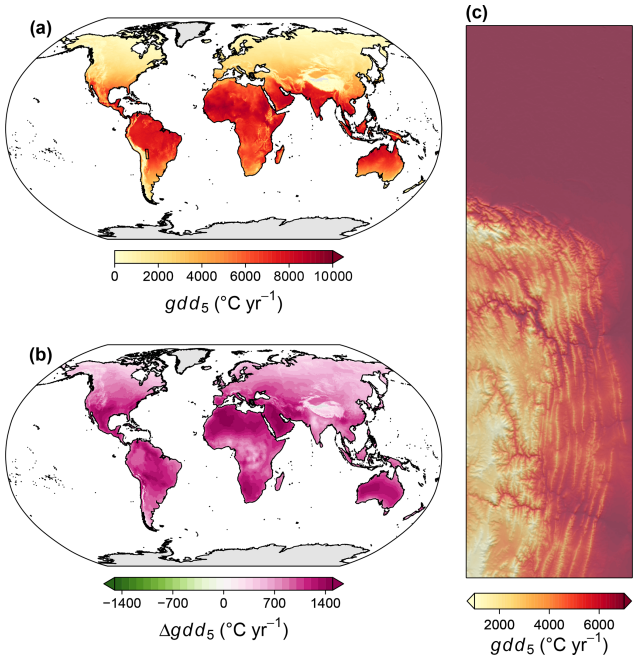

Figure 8. Overview of the spatiotemporal distribution of growing °C d with 5 °C baseline temperature (gdd_5). **(a)** Global map of the climatological mean of gdd_5 for the period 1981–2010. **(b)** Global map of the difference between climatological means of 2071–2100 and 1981–2010, assuming anthropogenic emissions to follow the shared socioeconomic pathway SSP370 and building on projections of the MPI-ESM 1-2-HR. **(c)** An exemplary high-resolution map of the climatological mean for the northeastern boundary region of the Andes. For the exact location, see the inset in panel **(a)**.

2.4 Output format and file organization

All downscaled layers are provided as georeferenced tiff files (GeoTIFF). GeoTIFF is a public domain metadata standard which allows georeferencing information to be embedded within a TIFF file. Identical to the CHELSA layers (Karger et al., 2017), maps are projected in World Geodetic System 1984 (EPSG 4326) and have a western extent of −180.0001388888°, a southern extent of −90.0001388888°, an eastern extent of 179.9998611111°, and a northern extent of 83.9998611111°. Their resolution is 0.0083333333° (30 arcsec), resulting in raster sizes of 20 880 × 43 200 cells. All GeoTIFF files are saved as integers with the compression option "deflate" and an internal scale and offset (see the Technical Specifications document on the CHELSA website). In order to read offset and scale correctly, the geospatial data abstraction library (GDAL, https://gdal.org, last access: 4 September 2020) version 2.2 or higher is needed; otherwise, they may have to be applied manually. All variables are time averages either representing the periods 1981–2010, 2011–2040, 2041–2070, or 2071–2100 (in the case of climatologies) or individual year–month combinations (in the case of time series data). Monthly time series range at least from 1980 to 2018, while the annual time series of swb ranges from 1981 to 2018. Climate variable and time period as well as SSP and Earth system model (if applicable) are encoded in the file names.

2.5 Software used

For the generation and validation of the climate layers, we relied on three open-source software environments. Most raster operations, such as averaging or calculating extrema, were executed with SAGA V.8.1 (Conrad et al., 2015); output GeoTIFFs were created with GDAL (https://gdal.org, last access: 4 September 2020); validation, visualization, as well as complex raster operations were implemented in the R environment (R Development Core Team, 2008). R packages used, in addition to those indicated above, included sp (Pebesma and Bivand, 2005), raster (Hijmans, 2019), and magick (Ooms, 2020).

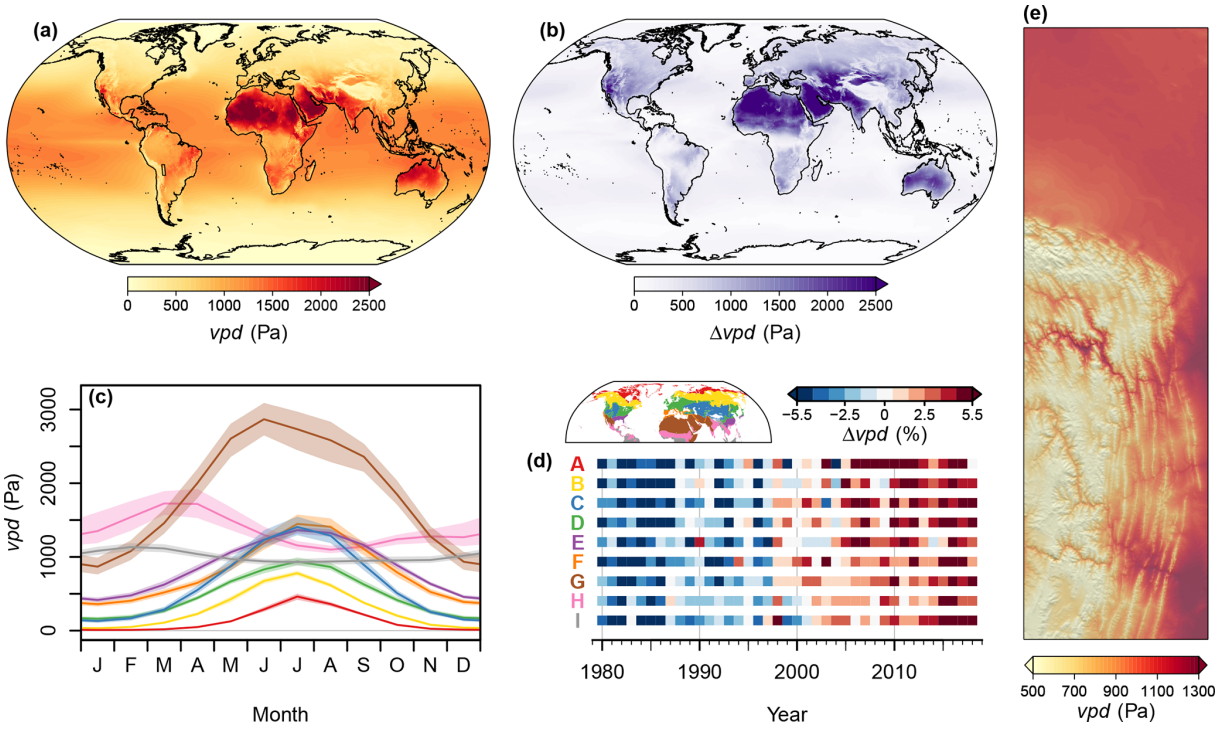

Figure 9. Overview of the spatiotemporal distribution of vapor pressure deficit (vpd). **(a)** Global map of the climatological mean for the period 1981–2010. **(b)** Global map of the range (max–min) of monthly vpd means for the period 1981–2010. **(c)** Seasonal cycle of vpd in the biomes of the Northern Hemisphere for the period 1981–2010. Polygons indicate the range from the 40th to 60th percentiles, and lines indicate medians. **(d)** Temporal change in annual mean vpd by biome. Shown are deviations in percent of the long-term (1980–2018) annual mean. Red (A) represents the polar and subpolar zone; yellow (B) represents the boreal zone; blue (C) represents dry midlatitudes; green (D) represents temperate midlatitudes; purple (E) represents subtropics with year-round rain; orange (F) represents subtropics with winter rain; brown (G) represents dry tropics and subtropics; pink (H) represents tropics with summer rain; grey (I) represents tropics with year-round rain. **(e)** An exemplary high-resolution map of the climatological mean of vpd for the northeastern boundary region of the Andes. For the exact location, see the inset in panel **(a)**.

3 Results

3.1 Spatiotemporal patterns

3.1.1 First-order climate layers

Near-surface relative humidity was highest in the polar regions and – to a lesser extent – at the Equator and lowest in parts of the subtropics, including northern Africa, the Arabian Peninsula, and northwestern Australia (Fig. 2a). The seasonal variation of hurs was most pronounced in the far north, for example, in northern Canada, but also along an east–west belt in subtropical Africa, roughly from the southern tip of the Red Sea to the Atlantic Ocean (Fig. 2b). In terms of Northern Hemisphere biomes, hurs was lowest in the dry tropics and subtropics, especially in May and June, and highest in the polar and subpolar zone, especially in January and February (Fig. 2c). Over the past 40 years, annual means of hurs varied in all Northern Hemisphere biomes, with consistent and clear trends of decreasing hurs (Fig. 2d). In the northeastern boundary region of the Andes, hurs tended to be higher at the northern edge of the Andes and around the eastern mountain tops than in the eastern lowlands and on the Andean Plateau (Fig. 2e).

Cloud area fraction was highest in the polar regions and in some equatorial regions, such as Indonesia, and lowest in parts of the subtropics, including northern and southern Africa and the Arabian Peninsula (Fig. 3a). The seasonal variation of clt was most pronounced in subtropical and monsoon regions, for example, on the Indian subcontinent (Fig. 3b). In terms of Northern Hemisphere biomes, clt was lowest in the dry tropics and subtropics, especially from June to August, and highest in the polar and subpolar zone, especially in May and October (Fig. 3c). For the past 40 years, substantial variations in annual mean clt are mapped in most Northern Hemisphere biomes, with more (e.g., temperate midlatitudes) or less (e.g., dry tropics and subtropics) apparent negative trends (Fig. 3d). In the northeastern boundary region of the Andes clt tended to be higher at the northern edge of the Andes and around the eastern mountain tops than in inner alpine valleys and on the Andean Plateau (Fig. 3e).

Near-surface wind speed was comparably high at the high latitudes, in coastal regions, in deserts, and in mountain sys-

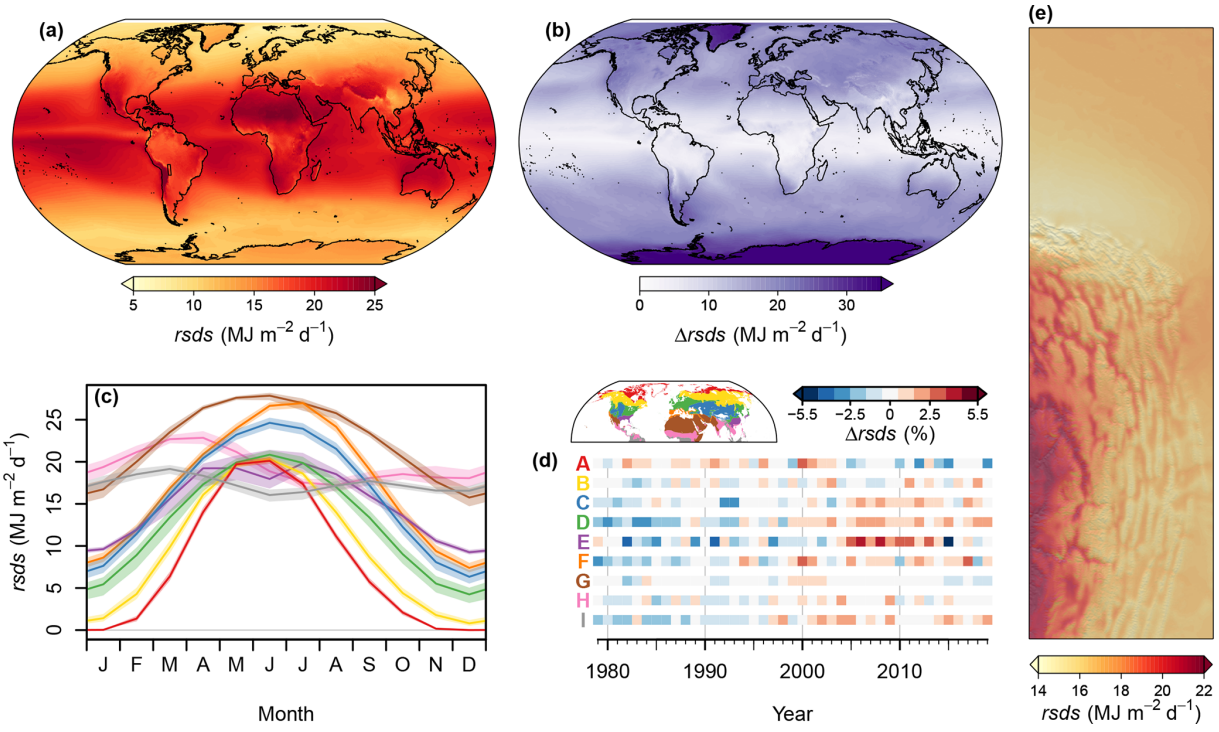

Figure 10. Overview of the spatiotemporal distribution of rsds. **(a)** Global map of the climatological mean for the period 1981–2010. **(b)** Global map of the range (max–min) of monthly rsds means for the period 1981–2010. **(c)** Seasonal cycle of rsds in the biomes of the Northern Hemisphere for the period 1981–2010. Polygons indicate the range from the 40th to 60th percentiles, and lines indicate medians. **(d)** Temporal change in annual mean rsds by biome. Shown are deviations in percent of the long-term (1979–2019) annual mean. Red (A) represents the polar and subpolar zone; yellow (B) represents the boreal zone; blue (C) represents dry midlatitudes; green (D) represents temperate midlatitudes; purple (E) represents subtropics with year-round rain; orange (F) represents subtropics with winter rain; brown (G) represents dry tropics and subtropics; pink (H) represents tropics with summer rain; grey (I) represents tropics with year-round rain. **(e)** An exemplary high-resolution map of the climatological mean of rsds for the northeastern boundary region of the Andes. For the exact location, see the inset in panel **(a)**.

tems and lowest at the Equator (Fig. 4a). In general, seasonal variations were relatively small, with the notable exceptions of seasonally variable sfcWind regions in a few, scattered regions such as Greenland and the Horn of Africa (Fig. 4b). In terms of Northern Hemisphere biomes, sfcWind was lowest in the tropics, with year-round rain, and highest in the polar and subpolar zone (Fig. 4c). For the past 40 years, substantial variations in annual mean sfcWind are mapped in Northern Hemisphere biomes (Fig. 4d). They show few persistent changes besides a slight increasing trend in the dry tropics and subtropics and a slight decreasing trend at the temperate midlatitudes. In the northeastern boundary region of the Andes, sfcWind tended to be highest on mountain tops, in the mideastern lowlands around the city of Santa Cruz de la Sierra, and above the lakes in the northern lowlands of the Amazon Basin (Fig. 4e).

3.1.2 Second-order climate layers

Frost change frequency was highest along a circumpolar belt at the temperate to high latitudes of the Northern Hemisphere (Fig. 5a) as well as in some mountain systems such as the Andes, while it was zero across most of the subtropics and tropics. Until 2071–2100 fcf is expected to decrease in particular in global mountain systems and across much of the northern half of the contiguous United States, central and eastern Europe, and southwestern Asia, while increasing frost change frequencies are expected for southeastern Canada, the Baltic countries, Belarus, Ukraine, Mongolia, and parts of northern and northeastern China, such as the Hengduan Mountains (Fig. 5b), indicating an increase in thawing events in these areas. In the western Himalayas, fcf was highest at intermediate elevations, and it showed a tendency to decrease towards valley bottoms as well as towards mountain peaks (Fig. 5c).

Snow cover days increased with latitude, with zero scd occurring across most of the subtropics and tropics, except for some mountain systems, e.g., the Himalayas (Fig. 6a). Until 2071–2100 scd are expected to decrease in all regions of the world that currently have snow cover days, except for Greenland and Antarctica. The strongest declines are expected for the northeastern contiguous United States and for eastern and

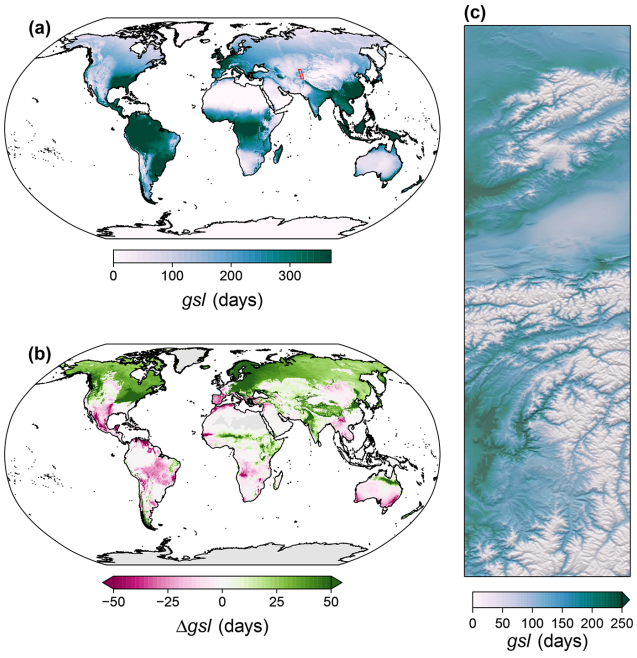

Figure 11. Overview of the spatiotemporal distribution of growing season length (gsl). **(a)** Global map of the climatological mean of gsl for the period 1981–2010. **(b)** Global map of the difference between climatological means of 2071–2100 and 1981–2010, assuming anthropogenic emissions to follow the shared socioeconomic pathway SSP370 and building on projections of the MPI-ESM 1-2-HR. **(c)** An exemplary high-resolution map of the climatological mean for the western edge of the Himalayas. For the exact location, see the inset in panel **(a)**.

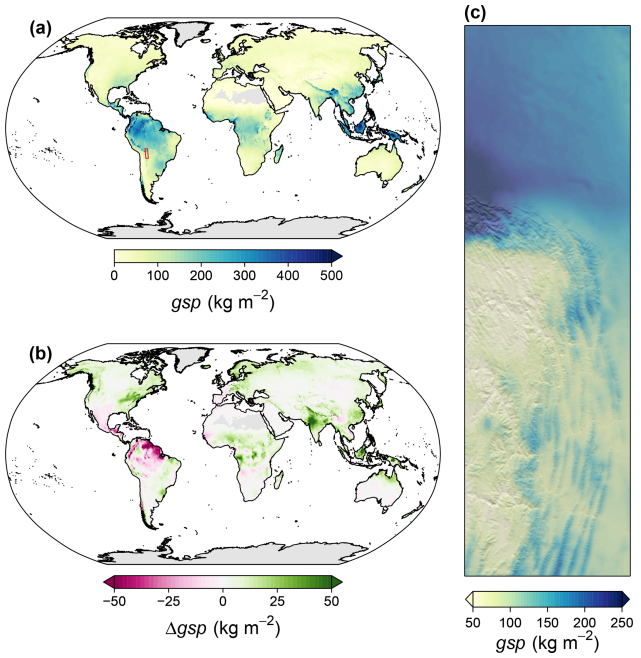

Figure 12. Overview of the spatiotemporal distribution of growing season precipitation (gsp). **(a)** Global map of the climatological mean of gsp for the period 1981–2010. **(b)** Global map of the difference between climatological means of 2071–2100 and 1981–2010, assuming anthropogenic emissions to follow the shared socioeconomic pathway SSP370 and building on projections of the MPI-ESM 1-2-HR. **(c)** An exemplary high-resolution map of the climatological mean for the northeastern boundary region of the Andes. For the exact location, see the inset in panel **(a)**.

northern Europe (Fig. 6b). In the western Himalayas, scd was positively associated with elevation (Fig. 6c).

Potential net primary productivity was highest in the tropics, for example, in the Amazon Basin, and lowest close to the poles and in arid regions, such as northern Africa (Fig. 7a). Until 2071–2100 npp is expected to increase across many of the northern high latitudes, in high mountain systems, and in the northwest of the Indian subcontinent. Decreasing npp is expected for the islands and the southern coast of the Caribbean Sea, for Central America, and for the coasts of the Mediterranean Sea (Fig. 7b). In the northeastern boundary region of the Andes, npp was highest in the northern lowlands of the Amazon Basin and lowest on the bottoms of dry inner alpine valleys (Fig. 7c).

Growing degree days with 5 °C baseline temperature (gdd_5) were highest in the tropics and subtropics and decreased towards the high latitudes (Fig. 8a). Until 2071–2100 gdd_5 is expected to increase in all regions of the world, except for Greenland and Antarctica. The strongest increases are expected for northern Africa and the Arabian Peninsula, Mexico, and western Australia (Fig. 8b). In the northeastern boundary region of the Andes, gdd_5 was highest in the northern lowlands of the Amazon Basin and in some inner alpine valleys, while they were lowest on high mountain peaks and the Andean Plateau (Fig. 8c).

The climatological mean of vpd was highest in dry subtropical regions, for example, northern Africa, the Arabian Peninsula, and central and western Australia. It was lowest in high mountain systems, such as the Himalayas, and the polar regions (Fig. 9a). The spatial patterns of seasonal variation in vpd were similar to those of the climatological mean (Fig. 9b). In terms of Northern Hemisphere biomes, vpd was lowest in the polar and subpolar zone, primarily from November to March, and highest in the dry tropics and subtropics, especially around June (Fig. 9c). Over the past 40 years annual mean vpd showed clearly increasing trends in all Northern Hemisphere biomes (Fig. 9d). In the northeastern boundary region of the Andes vpd showed a primary negative association with elevation, with the highest vpd in the lowlands and in some inner alpine valleys and the lowest vpd on mountain peaks and on the Andean Plateau (Fig. 9e).

rsds was highest in the subtropics and tropics, for example, northern Africa and the Arabian Peninsula, and decreased towards higher latitudes (Fig. 10a). The seasonal variation in rsds showed approximately opposite patterns, with the lowest seasonal variations in the tropics and the highest vari-

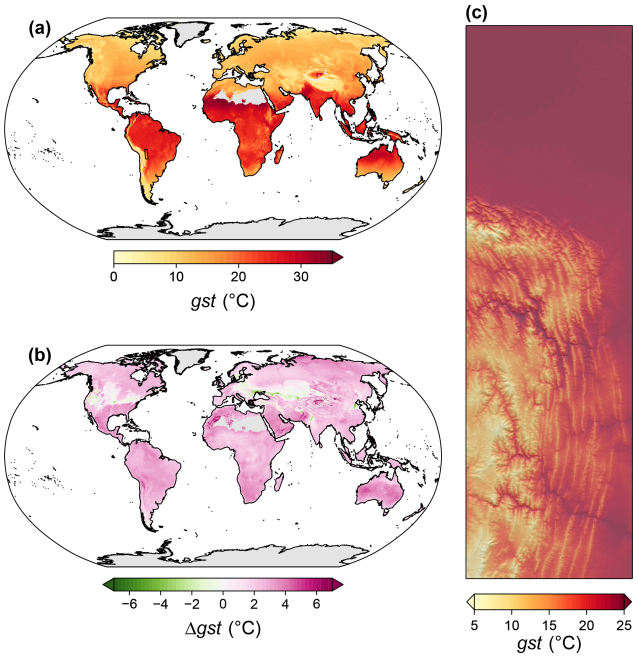

Figure 13. Overview of the spatiotemporal distribution of growing season temperature (gst). **(a)** Global map of the climatological mean of gst for the period 1981–2010. **(b)** Global map of the difference between climatological means of 2071–2100 and 1981–2010, assuming anthropogenic emissions to follow the shared socioeconomic pathway SSP370 and building on projections of the MPI-ESM 1-2-HR. **(c)** An exemplary high-resolution map of the climatological mean for the northeastern boundary region of the Andes. For the exact location, see the inset in panel **(a)**.

ations in Antarctica and Greenland (Fig. 10b). In terms of Northern Hemisphere biomes, rsds was lowest in the polar and subpolar zone, from November to January, and highest in the dry tropics and subtropics, especially around June (Fig. 10c). Over the past 40 years, annual mean rsds showed variable trends across Northern Hemisphere biomes: in several biomes, for example, in the tropics with year-round rain and in particular in the subtropics with year-round rain, rsds tended to increase (Fig. 10d), whereas in the polar and subpolar zone rsds tended to decrease. In the northeastern boundary region of the Andes rsds tended to be highest on the Andean Plateau and high-elevation mountain peaks and lowest on the northern edge of the Andes and on the western slopes on the western edge of the Andes (Fig. 10e).

3.1.3 Third-order climate layers

Growing season length was highest in the tropics, where it typically covered the entire year, and lowest in polar areas, in particular in Greenland and Antarctica, in arid areas, e.g., northern Africa, and in high mountain systems such as the Himalayas, the Rockies, or the high Andes (Fig. 11a). Until 2071–2100 gsl is expected to increase across most of the temperate to high latitudes of the Northern Hemisphere and in the greater Himalayan region, but also in parts of northern Australia and central to eastern Africa, such as Kenya and Ethiopia. Declining growing season lengths are expected for Mexico and the southwestern US and across much of tropical South America, Spain, Morocco, and southern Australia (Fig. 11b). In the western Himalayas gsl was negatively associated with elevation (Fig. 11c).

Growing season precipitation was highest in the tropics and in the monsoon region of southern China and comparably low in desert regions around the globe and at the higher latitudes, except for some coastal areas such as western North America (Fig. 12a). Until 2071–2100 gsp is expected to increase along the coasts of western and eastern North America, across most of Eurasia, in Oceania, and in northern Australia. Decreases are expected in particular in central and tropical America and in the Mediterranean region, in western Africa, and in southern Australia (Fig. 12b). In the northeastern boundary region of the Andes, gsp was highest in the northern lowlands of the Amazon Basin and in particular at the northern edge of the Andes, while it was lowest on the Andean Plateau (Fig. 12c).

Growing season temperature was highest in the tropics and subtropics and decreased towards the high latitudes (Fig. 13a). Until 2071–2100 gst is expected to increase in almost all regions of the world with growing seasons, with the steepest increases, for example, in Mauritania. Decreasing growing season temperatures are expected, for example, from southern Sweden and over southern Ukraine to Kazakhstan (Fig. 13b). In the northeastern boundary region of the Andes, gst was highest in the lowlands and in some inner alpine valleys, while it was lowest on high-elevation mountain peaks and on the Andean Plateau (Fig. 13c).

Potential evapotranspiration was highest in the subtropics, such as northern Africa, and decreased towards higher latitudes and – to a lesser extent – towards the tropics (Fig. 14a). The seasonal variation of pet was also highest in the subtropics, but its minimum was in the tropics, and in the polar region it was intermediate (Fig. 14b). In terms of Northern Hemisphere biomes, pet was lowest in the polar and subpolar zone, from December to February, and highest in the dry tropics and subtropics, especially from May to July (Fig. 14c). For the past 40 years, an increasing trend of annual mean pet is mapped in all Northern Hemisphere biomes (Fig. 14d). In the northeastern boundary region of the Andes pet showed a negative association with elevation, with the lowest pet on high-elevation mountain peaks and on the Andean Plateau and the highest values in some inner alpine valleys and in the mideastern lowlands around the city of Santa Cruz. However, pet was also relatively low in the lowlands at the northern edge of the Andes, where clt and hurs were high and sfcWind and rsds were low (Fig. 14e).

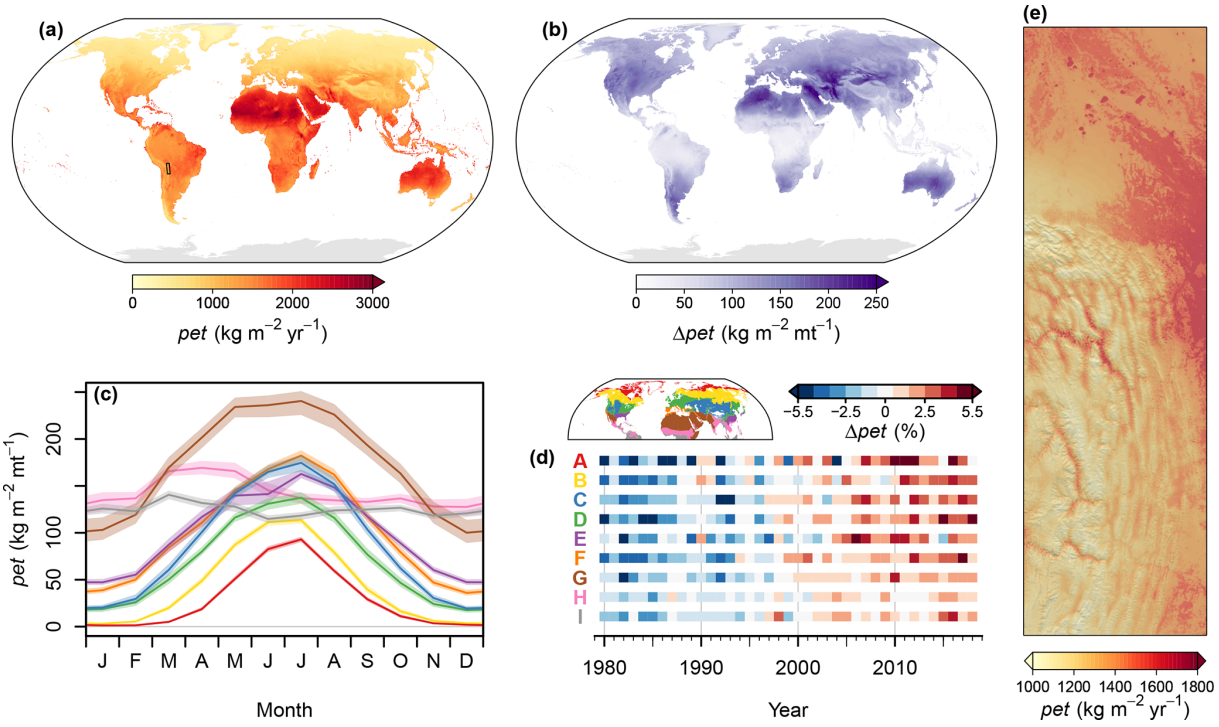

Figure 14. Overview of the spatiotemporal distribution of potential evapotranspiration (pet). **(a)** Global map of the climatological mean for the period 1981–2010. **(b)** Global map of the range (max–min) of monthly pet means for the period 1981–2010. **(c)** Seasonal cycle of pet in the biomes of the Northern Hemisphere for the period 1981–2010. Polygons indicate the range from the 40th to 60th percentiles, and lines indicate medians. **(d)** Temporal change in annual mean pet by biome. Shown are deviations in percent of the long-term (1980–2018) annual mean. Red (A) represents the polar and subpolar zone; yellow (B) represents the boreal zone; blue (C) represents dry midlatitudes; green (D) represents temperate midlatitudes; purple (E) represents subtropics with year-round rain; orange (F) represents subtropics with winter rain; brown (G) represents dry tropics and subtropics; pink (H) represents tropics with summer rain; grey (I) represents tropics with year-round rain. **(e)** An exemplary high-resolution map of the climatological mean of pet for the northeastern boundary region of the Andes. For the exact location, see the inset in panel **(a)**.

3.1.4 Fourth-order climate layers

Climate moisture index was highest in parts of the tropics and in some mountain systems, especially in those located close to the coasts, and lowest in northern Africa and the Arabian Peninsula (Fig. 15a). The seasonal variation in cmi was highest in the tropics and subtropics and in some coastal mountain systems such as the Pacific Northwest of North America, while in high-latitude lowlands, variation was comparably low (Fig. 15b). In terms of Northern Hemisphere biomes, cmi was lowest in the dry tropics and subtropics, from May to July, and highest in the tropics with year-round rain, especially in May and June (Fig. 15c). For the past 40 years, substantial variations in annual mean cmi were observed in Northern Hemisphere biomes, without clear temporal trends (Fig. 15d). However, cmi showed a tendency to decrease in the dry tropics and subtropics. In the northeastern boundary region of the Andes cmi was mostly negative, in particular in inner alpine valleys, although at the northern edge of the Andes and in the lowlands of the Amazon Basin cmi was mostly positive (Fig. 15e).

3.1.5 Fifth-order climate layers

Site water balance was typically neutral to positive in the tropics and at temperate to high latitudes, while it was mostly negative elsewhere, most distinctly so in northern Africa and the Arabian Peninsula (Fig. 16a). For the past 40 years, substantial variations in annual mean swb are mapped in Northern Hemisphere biomes, mostly without clear temporal trends (Fig. 16b). However, swb did show a tendency to decrease in the dry tropics and subtropics. In the northeastern boundary region of the Andes and the surrounding lowlands, swb was mostly negative, in particular in inner alpine valleys, while it was slightly positive close to the northern edge of the Andes (Fig. 16c).

3.2 Validation and comparisons

3.2.1 Station data

CHELSA-BIOCLIM+ layers showed a good fit with the station measurements, especially in the case of gdd_5, vpd, hurs, fcf, and cmi (Table 2). Pearson correlation coefficients (r)

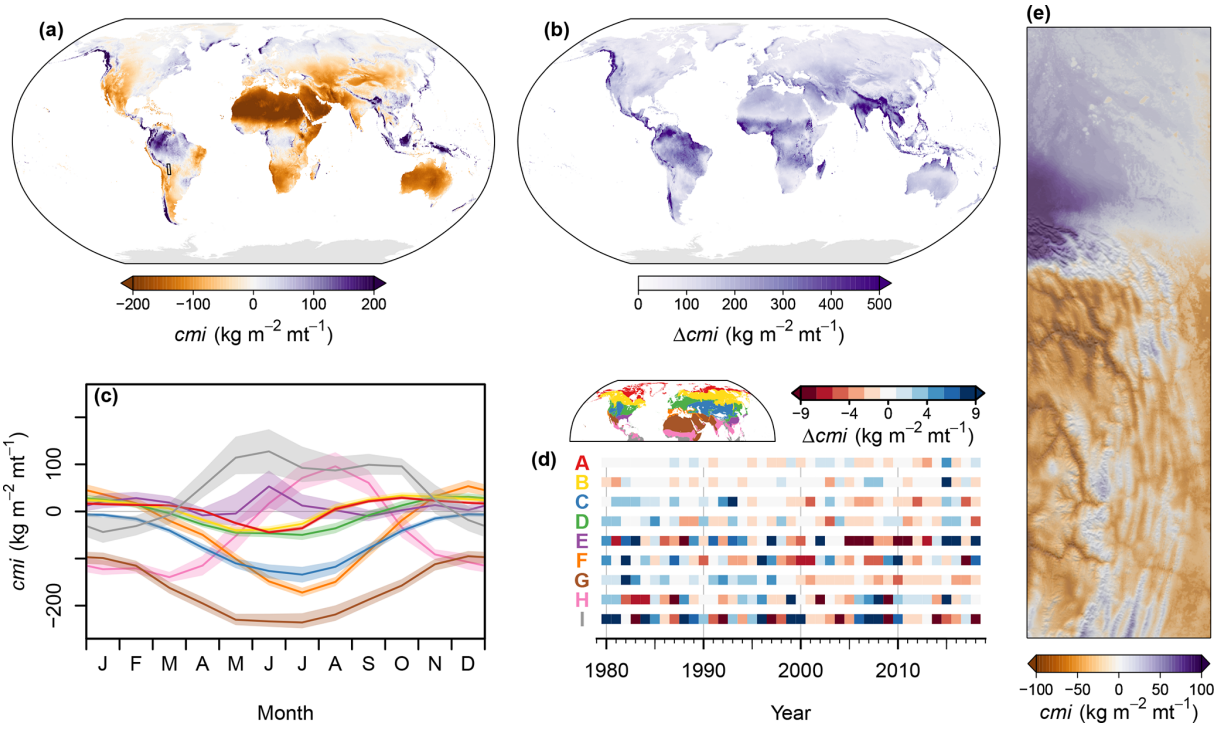

Figure 15. Overview of the spatiotemporal distribution of climate moisture index (cmi). **(a)** Global map of the climatological mean for the period 1981–2010. **(b)** Global map of the range (max–min) of monthly cmi means for the period 1981–2010. **(c)** Seasonal cycle of cmi in the biomes of the Northern Hemisphere for the period 1981–2010. Polygons indicate the range from the 40th to 60th percentiles, and lines indicate medians. **(d)** Temporal change in annual mean cmi by biome. Shown are deviations in percent of the long-term (1980–2018) annual mean. Red (A) represents the polar and subpolar zone; yellow (B) represents the boreal zone; blue (C) represents dry midlatitudes; green (D) represents temperate midlatitudes; purple (E) represents subtropics with winter rain; orange (F) represents subtropics with year-round rain; brown (G) represents dry tropics and subtropics; pink (H) represents tropics with summer rain; grey (I) represents tropics with year-round rain. **(e)** An exemplary high-resolution map of the climatological mean of cmi for the northeastern boundary region of the Andes. For the exact location, see the inset in panel **(a)**.

were high ($r > 0.85$), across all temporal aggregations evaluated, for scd, gdd_5, vpd, and cmi, and at least reasonably high ($r > 0.80$) for hurs and fcf. For sfcWind, correlations were lowest, yet still acceptable, with $r \geq 0.74$. For most evaluated variables, r was similar when evaluated for monthly and annual climatologies, with the highest differences found for pet (r equalled 0.79 and 0.87 for annual and monthly climatologies, respectively). When estimated from monthly match-ups, r was generally lower. Over the evaluated stations, biases for annual climatologies ranged between ±2 % and 25 % of the station means, except for clt (on average 18 % too low, in absolute terms) and in particular scd (on average 38 d too high). MAE and RMSE were rather low for variables with comparably high r and low bias, such as hurs (MAE of 10.81 % for annual climatologies), and comparably high especially for variables with high bias, such as scd (MAE of 42.78 d).

Compared to station-based interpolations, CHELSA-BIOCLIM+ variables showed similar or higher performance for hurs, vpd, pet, and cmi and somewhat lower performance for sfcWind (Table 2). For annual climatologies of sfcWind, CHELSA-BIOCLIM+ grids showed lower correlation (r equalled 0.77 compared to 0.84 for station-based interpolations) and higher error (MAE equalled 0.72 compared to 0.53 for station-based interpolations). For hurs, vpd, pet, and cmi, on the other hand, MAE estimates for CHELSA-BIOCLIM+ layers were lower (−17.72 %, −338.17 Pa, $-11.86\,kg\,m^{-2}\,mt^{-1}$, and $-8.73\,kg\,m^{-2}\,mt^{-1}$, respectively), and r was similar or higher (+0.24, +0.06, +0.13, and −0.01, respectively) compared to the corresponding metrics for station-based interpolations.

Mean absolute error of CHELSA-BIOCLIM+ variables showed variable distributions in space. For hurs, MAE was high in Europe and Southeast Asia and comparably low in western North America and temperate to boreal Asia (Fig. 17a). For fcf, MAE was particularly high for an area extending from southeastern Europe eastwards into central Asia, while it was low for the subtropics and tropics (Fig. 17d). For gdd_5, elevated MAE was mainly found in the subtropics and tropics, especially in northern Mexico and at the northern edge of the Andes (Fig. 17f). For clt, sfcWind, pet, and cmi, the patterns were roughly uniform, although

Table 2. Validation results for the nine evaluated variables. r represents the Pearson correlation coefficient; MAE stands for mean absolute error; RMSE stands for root mean squared error; mean indicates the averages of station measurements; bias represents the average difference between gridded estimates and station measurements. Units are as reported in the methods.

Variable	Aggregation	Origin	Validation data	r	MAE	RMSE	Mean	Bias	Stations
hurs	Climat. mean[1]	This study	GSOD	0.90	10.81	11.84	69.62	−10.00	4412
hurs	Climat. month	This study	GSOD	0.88	11.45	12.71	69.68	−10.03	5702
hurs	Monthly	This study	GSOD	0.84	11.91	13.45	69.72	−10.03	17316
hurs	Climat.[1] mean	Station-based[2]	GSOD	0.66	28.53	30.44	69.11	28.51	4143
clt	Climat.[1] mean	This study	HadISD	0.87	18.07	19.21	55.76	−18.03	5095
clt	Climat.[1] month	This study	HadISD	0.86	18.12	19.70	55.87	−17.94	5989
clt	Monthly	This study	HadISD	0.79	18.01	20.66	55.09	−17.00	8323
sfcWind	Climat.[1] mean	This study	GSOD	0.77	0.72	0.94	3.38	0.05	4482
sfcWind	Climat.[1] month	This study	GSOD	0.78	0.76	1.00	3.37	0.06	5782
sfcWind	Monthly	This study	GSOD	0.74	0.87	1.17	3.33	0.14	17385
sfcWind	Climat.[1] mean	Station-based[2]	GSOD	0.84	0.53	0.74	3.28	−0.01	4223
fcf	Climat.[1] mean	This study	GSOD	0.82	19.76	27.26	50.99	−4.59	4101
scd	Climat.[1] mean	This study	GSOD	0.91	42.78	62.01	50.69	38.09	2283
gdd_5	Climat.[1] mean	This study	GSOD	0.99	159.14	239.16	3358.40	−67.00	4085
vpd	Climat.[1] mean	This study	GSOD	0.91	177.01	219.18	582.36	135.59	4143
vpd	Climat.[1] month	This study	GSOD	0.93	194.56	255.94	599.04	194.56	5702
vpd	Monthly	This study	GSOD	0.92	205.82	278.16	598.43	134.80	17316
vpd	Climat.[1] mean	Station-based[2]	GSOD	0.85	515.18	579.60	595.40	−515.04	4143
pet	Climat.[1] mean	This study	FAOCLIM	0.79	19.84	24.12	120.77	6.18	4247
pet	Climat.[1] month	This study	FAOCLIM	0.87	21.70	27.03	120.77	6.18	4206
pet	Climat.[1] mean	Station-based[2]	FAOCLIM	0.66	31.70	37.04	121.16	20.30	4050
cmi	Climat.[1] mean	This sutdy	FAOCLIM	0.88	27.35	40.50	−27.78	−2.94	4207
cmi	Climat.[1] month	This study	FAOCLIM	0.91	34.24	55.07	−21.78	−2.94	4166
cmi	Climat.[1] mean	Station-based[2]	FAOCLIM	0.89	36.08	45.71	−23.74	−21.01	4011

[1] Climatology for the period 1981–2010. [2] Derived from WorldClim v2.0 and the Global Aridity Index and Potential Evapotranspiration Database version 3 (Fick and Hijmans, 2017; Zomer et al., 2022).

some regions showed a somewhat elevated error, for example, Niger for clt or Mongolia for pet and cmi (Fig. 17b, c, h, i). For scd and vpd, which had a comparably high bias (Table 2), MAE showed a latitudinal pattern that was roughly proportional to the primary pattern of the variable (Fig. 17e, g).

Pearson correlation coefficients between station measurements and evaluated CHELSA-BIOCLIM+ variables varied with season and between years. Seasonal variations were particularly pronounced for hurs, where r was below 0.8 for January and December and above 0.9 from April to October (Fig. 18a). For sfcWind and pet, a clear seasonal signal in r also existed, but the highest correlations ($r>0.8$ and $r>0.9$, respectively) were found from November to February and the lowest correlations in July, for sfcWind ($r = 0.72$), and August, for pet ($r = 0.78$). For vpd and cmi, on the other hand, seasonal variations were comparably small. Interannual variations in Pearson correlation coefficients were pronounced for clt and sfcWind, while they were relatively small for vpd and hurs (Fig. 18b). Apart from the seasonal variations, r for clt and sfcWind remained relatively stable between 1980 and 1995 (average 1980–1995 r was 0.74 and 0.82 for sfcWind and clt, respectively). Between 1995 and the early 2000s, r declined for both variables before it started increasing again until about 2010. After that, r for both variables declined a second time until the end of the time series (average 2010-to-time series end r equalled 0.72 and 0.76 for sfcWind and clt, respectively).

3.2.2 Gridded data

In the Himalayan region, the spatial patterns of CHELSA-BIOCLIM+ variables were generally similar to those of the corresponding layers from station-based interpolations and weather research and forecasting simulations, although some exceptions existed. The spatial patterns of hurs were comparably variable among products, with the highest correlation between CHELSA-BIOCLIM+ and WRF ($r = 0.68$, Fig. 19a–c). For sfcWind, the large-scale patterns were quite similar, especially between CHELSA-BIOCLIM+ and WRF, but the fine-scale structures were resolved in higher detail in the CHELSA-BIOCLIM+ layers, explaining why the correlation between station-based interpolations and WRF was highest for wind speed (Fig. 19d–f). For vapor pres-

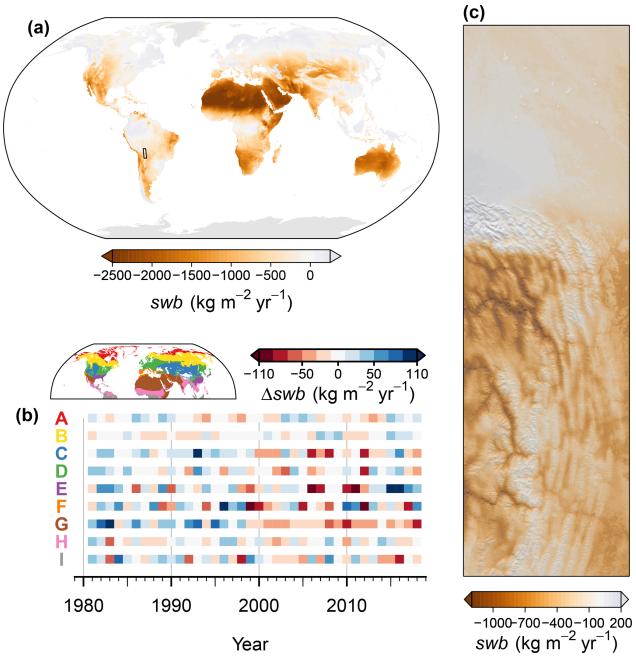

Figure 16. Overview of the spatiotemporal distribution of site water balance (swb): **(a)** global map of the climatological mean of swb for the period 1981–2010; **(b)** temporal change in annual mean swb by biome. Shown are deviations in percent of the long-term (1980–2018) annual mean. Red (A) represents the polar and subpolar zone; yellow (B) represents the boreal zone; blue (C) represents dry midlatitudes; green (D) represents temperate midlatitudes; purple (E) represents subtropics with winter rain; orange (F) represents subtropics with year-round rain; brown (G) represents dry tropics and subtropics; pink (H) represents tropics with summer rain; grey (I) represents tropics with year-round rain. **(c)** An exemplary high-resolution map of the climatological mean of swb for the northeastern boundary region of the Andes. For the exact location, see the inset in panel **(a)**.

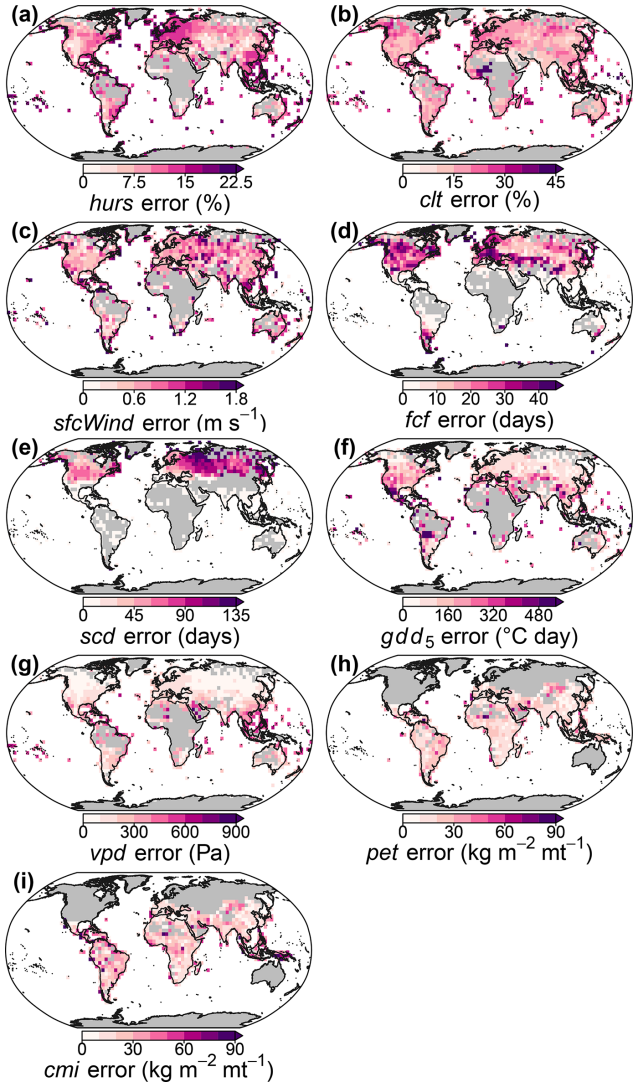

Figure 17. Spatial distribution of validation errors: global maps of mean absolute errors between 1981–2010 climatological means of nine CHELSA-BIOCLIM+ variables and corresponding averages of station estimates. Note that for pet **(h)** and cmi **(i)**, station data are representative for the period 1961–1990, and thus time periods only partially overlap.

sure deficit, the patterns between all the products were very similar (Fig. 19g–i). In the case of rsds, the CHELSA-BIOCLIM+ layer showed the most pronounced fine-scale patterns, and its large-scale patterns were similar to those in the WRF layer ($r = 0.73$ between CHELSA-BIOCLIM+ and WRF). The patterns of WorldClim's solar radiation, on the other hand, were strikingly different compared to the former two products ($r < 0$ for both comparisons, Fig. 19j–l). For pet, large-scale patterns between the three products were generally similar, although absolute values were somewhat lower for CHELSA-BIOCLIM+ and more fine-scale structures were visible (Fig. 19m–o). In the case of cmi the patterns were generally similar (Fig. 19m–o). Along the southern edge of the Himalayas, the large-scale patterns between CHELSA-BIOCLIM+ and WRF were somewhat more similar than those between CHELSA-BIOCLIM+ and station-based interpolations.

4 Data availability

The CHELSA-BIOCLIM+ dataset consists of 4006 single-layer GeoTIFF files, representing averages, extrema, and ranges of the 15 climate-related variables for different time points (1979 to 2100) and periods (monthly to 30-year averages). The GeoTIFF files are stored on a S3 cloud server that can be accessed over EnviDat (https://doi.org/10.16904/envidat.332; Brun et al., 2022) by clicking on the "CHELSA-BIOCLIM+" box in the "Data and resources" tab and at https://chelsa-climate.org/ (last access: 12 December 2022) by clicking on "Version 2.1" under "Downloads". This file browser contains the four folders "an-

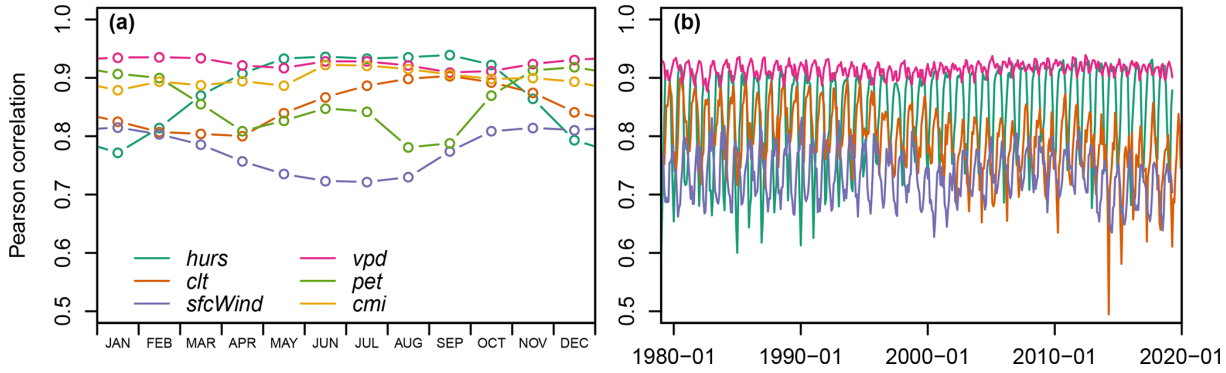

Figure 18. Seasonal and interannual distribution of correspondence: **(a)** Pearson correlation coefficients between CHELSA-BIOCLIM+ variables and corresponding averages of station measurements for hurs, clt, sfcWind, vpd, pet, and cmi for each 1981–2010 climatological month. Note that for pet (purple) and cmi (yellow), station data are representative for the period 1961–1990, and thus time periods only partially overlap. **(b)** Pearson correlation coefficients between CHELSA-BIOCLIM+ variables and corresponding averages of station measurements for hurs, clt, sfcWind, and vpd for each month in the time series. The same colors are used as in panel **(a)**.

nual", "daily", "monthly", and "climatologies", within which the CHELSA-BIOCLIM+ data are organized in the following way.

The folder "annual" contains the subfolder "swb", which contains annual layers of swb.

The folder "daily" contains no data of the CHELSA-BIOCLIM+ dataset.

The folder "monthly" contains (among folders from other datasets) the subfolders "clt", "cmi", "hurs", "pet", "rsds", "sfcWind", and "vpd", which contain monthly layers for clt, cmi, hurs, pet, rsds, sfcWind, and vpd, respectively.

The folder "climatologies" contains four subfolders, "1981–2010", "2011–2040", "2041–2070", and "2071–2100", which represent the different time periods for which climatologies are representative.

In the subfolder "1981–2010" the sub-subfolders "clt", "cmi", "hurs", "pet", "rsds", "sfcWind", and "vpd" contain 1981–2010 averages of clt, cmi, hurs, pet, rsds, sfcWind, and vpd, respectively, for each month. The sub-subfolder "bio" contains (among files from other datasets) climatological means, maxima, minima, and annual ranges for clt, cmi, hurs, pet, rsds, sfcWind, and vpd and climatological means for fcf, gdd (with 0, 5, and 10 °C baseline temperature, i.e., "gdd0", "gdd5", "gdd10", respectively), gsl, gsp, gst, npp, scd, and swb.

The subfolders "2010–2040", "2041–2070", and "2071–2100" each contain one sub-subfolder per Earth system model considered (i.e., the sub-subfolders "GFDL-ESM4", "IPSL-CM6A-LR", "MPI-ESM1-2-HR", "MRI-ESM2-0", and "UKESM1-0-LL"). Each of these combinations between period and Earth system model contains three sub-sub-subfolders representing the three SSPs (i.e., the sub-sub-subfolders "ssp126", "ssp370", and "ssp585"); each of these combinations between period, Earth system model, and SSP contains a sub-sub-sub-subfolder "bio" that contains (among files from other datasets) climatological means for fcf, gdd (with 0, 5, and 10 °C baseline temperature), gsl, gsp, gst, npp, and scd.

More information on naming and settings of the GeoTIFF files (grid structure, unit, scale and offset parameters) can be found in the subsection "2.4 Output format and file organization" and in the Technical Documentation PDF that can be found at https://doi.org/10.16904/envidat.332 in the "CHELSA-BIOCLIM+ Technical Documentation" box in the "Data and resources" tab. Monthly and annual layers of the time-series variables will occasionally be added to the CHELSA-BIOCLIM+ dataset to extend the time period covered to the most recent years.

5 Discussion

Climate data at high spatiotemporal resolution for current conditions and for the decades ahead of us are crucial for filling the gaps in our understanding of climate-change impacts on the Earth system. Here, we provide a dataset of biologically meaningful, essential climate, and environmental variables, combining state-of-the-art input data with a mechanistic downscaling methodology. The provided gridded layers offer unprecedented spatiotemporal resolution and high validation accuracy. Characterizing bioclimate comprehensively beyond temperature and precipitation makes our dataset particularly relevant for studying biological processes (Bojinski et al., 2014; Woodward, 1987; Neilson, 1995). The open-access dataset CHELSA-BIOCLIM+ will stimulate research on climate-change impact on physical and ecological processes.

Comprehensive information on climate beyond temperature and precipitation enables better characterization of various Earth system processes, and biological processes in particular, where the balance between water supply and energy demand is central (Woodward, 1987). Our time-series variables related to water availability (hurs, vpd, pet, cmi) and

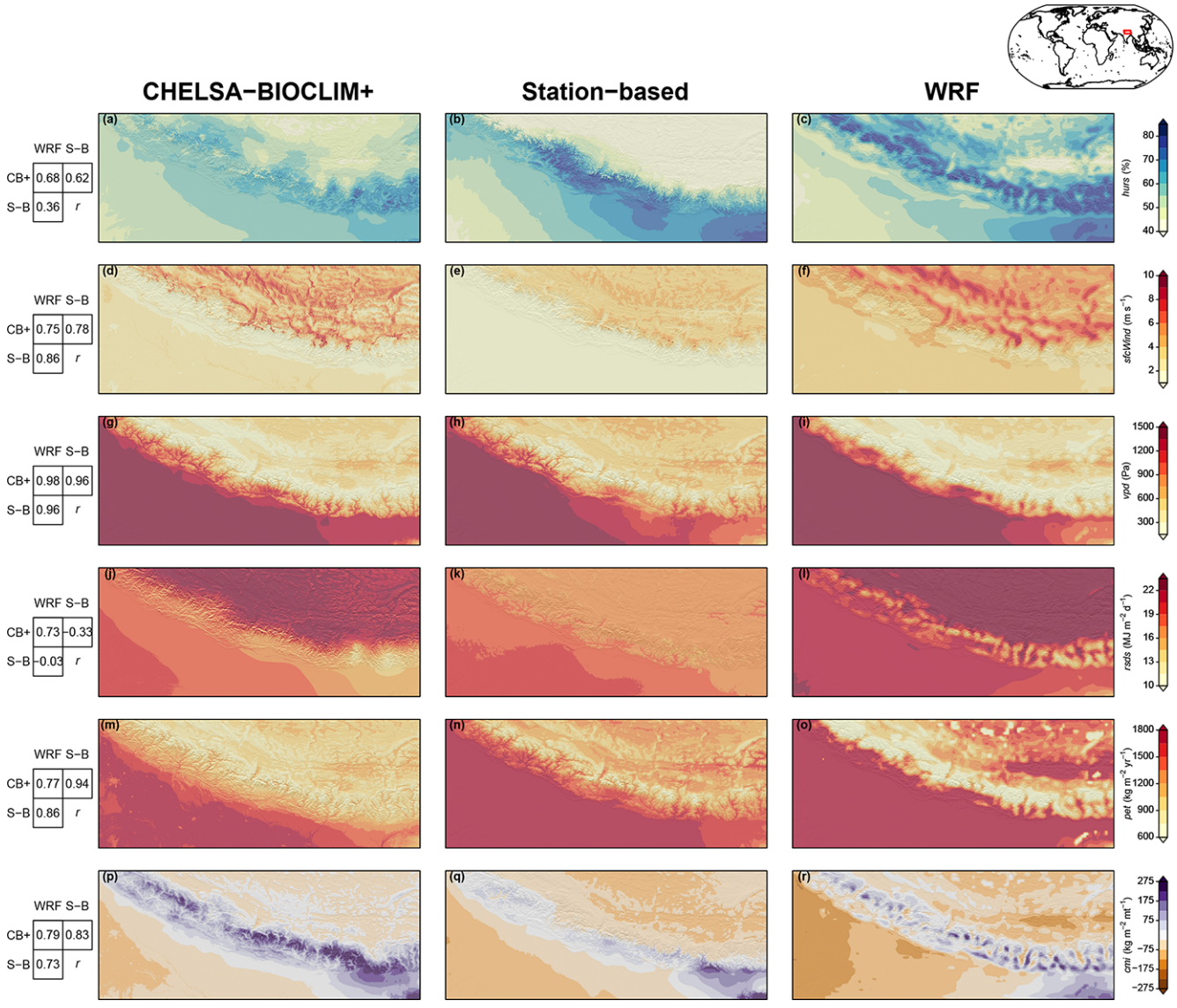

Figure 19. Spatial patterns in a data-poor region – a comparison with existing products. CHELSA-BIOCLIM+ variables are compared with equivalents from station-based interpolation and form a weather research and forecasting (WRF) model for hurs **(a–c)**, sfcWind **(d-f)**, vpd **(g–i)**, rsds **(j–l)**, pet **(m–o)**, and cmi **(p–r)** in the Himalayan region (see the inset map in the top right). On the left, for each variable pairwise Pearson correlation coefficients are shown for the mapped area, between CHELSA-BIOCLIM+ (CB+), the WRF model, and station-based interpolations (S–B). Station-based interpolations are derived from WorldClim v2.0 and the Global Aridity Index and Potential Evapotranspiration Database version 3 (Fick and Hijmans, 2017; Zomer et al., 2022); the WRF simulation considered was the High Asia Refined analysis v1 (Maussion et al., 2011, 2014).

incoming solar energy (clt, rsds) matched particularly well with validation data. Moreover, they showed low error in comparison to estimates derived from station-based interpolations. They can thus provide valuable inputs to a variety of downstream analyses such as analyzing the distribution of leaf area (Grier and Running, 1977; Iio et al., 2014), primary productivity (Gholz, 1982; Aguilos et al., 2021), or plant functional type-based biomes (Neilson, 1995; Schultz, 2005). For swb, suitable data for direct validation are scarce. However, given that only an additional estimate of soil water bucket size went into the calculation of this variable, we can expect that its performance will be comparable to the input variables it was computed from. rsds was not validated here, but Karger et al. (2022) demonstrated that, on a daily basis, global rsds estimates matched very well with in situ measurements ($r = 0.89$). Moreover, in the Himalayan region, the spatial pattern of rsds matched well with dynamically downscaled WRF outputs (Fig. 19). A key strength of the CHELSA-BIOCLIM+ product therefore lies in the provision of accurate, high-resolution, global time series of climate-

related variables describing the true availability of water and solar energy.

Combining input data from reanalysis with mechanistic downscaling approaches allows for robust estimates, in particular in remote areas. So far, climate data used in macroecological analyses have often relied on station-based interpolations (Bobrowski et al., 2021). While such data may be accurate in regions that have a dense network of field stations, such as Europe and North America (Hijmans et al., 2005), they are much less reliable in remote areas and/or in complex terrain (Karger et al., 2017). The CHELSA approach, on the other hand, uses gridded reanalysis data that account for physical mesoscale atmospheric processes and physical consistency (Hersbach et al., 2020) and further considers major orographic effects such as the shading of terrain or wind exposure (e.g., for hurs, clt, and pet; see the methods). Given the lack of field stations in remote areas, the extent of these improvements is likely not fully mirrored in the validation results, although our comparison among different products in the Himalayan region highlights that CHELSA-BIOCLIM+ layers generally compare well to alternative products. Moreover, CHELSA-based estimates of temperature and precipitation, which fully or partially underlie most variables presented here, have repeatedly been shown to be better suited than station-based interpolations for ecological modeling in the remote Himalayas (Datta et al., 2020; Suwal et al., 2018). It may therefore be expected that the CHELSA-BIOCLIM+ product will be particularly advantageous in remote areas.

Generating a comprehensive global set of high-resolution climate-related variables requires making generalizing assumptions that can compromise the accuracy of some estimates. Specifically, our projected variables providing current and future estimates are sensitive to bias, since simple models were preferred for making robust projections (Levins, 1966). As highlighted by the validation, our estimates of scd overestimated station-based measurements by about 1 month in regions with snow. These differences may arise from generating estimates of daily tas, tasmin, tasmax, and pr from monthly averages by means of spline interpolation, which results in a more gradual seasonal evolution of temperature and precipitation than observed in natural weather patterns. Moreover, for the computation of scd, contributing factors such as solar radiation were ignored. Similarly, the model to generate estimates for gsl, gsp, and gst only contained a simplistic implementation of soil water processes (Paulsen and Körner, 2014), and the Miami model to generate estimates for npp ignored soil conditions and solar radiation entirely. However, the approaches used to generate projected variables were not primarily selected for their accuracy but for their generalism (Levins, 1966) to be applicable under current and projected future conditions and to avoid overfitting. Despite significant advances during the past years (Kawamiya et al., 2020), Earth system models are still not capable of fully resolving mesoscale weather processes, and thus they are primarily suited to studying long-term changes in climate rather than possible weather patterns (Held et al., 2019; Yukimoto et al., 2019; Gutjahr et al., 2019; Boucher et al., 2020). Relative to our time-series variables, our projected variables may therefore not offer the same high accuracy for the recent past, but they approximate climate-change impact on fundamental biological and ecological quantities, such as potential net primary productivity, and make them directly comparable for a variety of possible future conditions, building on the most accurate global prognoses that are currently available (Eyring et al., 2016).

The validation also revealed inaccuracies for the time-series variable sfcWind. Although in the remote Himalaya region the sfcWind grids of CHELSA-BIOCLIM+ compared well to dynamically downscaled sfcWind from WRF, the correspondence to station measurements was weaker than for gridded data from station-based interpolations. Moreover, the monthly Pearson correlation coefficients between grids and station measurements declined somewhat for recent years. A reason for the higher correlation of the station-based interpolations might be that the station measurements we used here for validation largely overlap with their input data (Fick and Hijmans, 2017), and thus they are expected to perform well in our validation. Downscaling wind fields from ERA5, on the other hand, is challenging, as wind inherently contains a high variance that can be reconstructed to a limited degree even with the most sophisticated downscaling approaches (Pryor and Hahmann, 2019). Perhaps even more importantly, wind fields from reanalysis by themselves are of limited accuracy. Global meteorological stations indicate that wind speed has been declining from the 1980s until around 2010 and has recovered afterwards. In reanalysis products, however, this striking pattern is hardly reproduced (Zeng et al., 2019). We will keep updating and improving the CHELSA family of climate data products, and this is especially true for sfcWind should better input data become available.

In conclusion, CHELSA-BIOCLIM+ is a comprehensive spatial and temporal dataset of 15 climate-related variables including both, time series for the past 40 years and future projections building on several SSPs and Earth system models. Besides the climatological statistics provided, these data may be used to compute additional summaries, for example, interannual variabilities of cmi, which are important factors determining ecosystem structure in the dry midlatitudes, subtropics and tropics (Schultz, 2005). Moreover, the downscaling pipeline developed here opens new perspectives to develop near-real-time risk assessments when regularly updated and combined with machine learning and increasingly available global phenomenological datasets. The higher temporal resolution and the more proximal variables included in the CHELSA-BIOCLIM+ product will allow for a more detailed characterization of climate-related conditions and, in turn, a deeper understanding of their impact on key environmental processes.

Author contributions. PB, DNK, NEZ, and LP conceived the general idea of the paper. PB and DNK generated the dataset. CH conducted the validation with the support of PB and DNK. PB led the writing of the manuscript. All the authors significantly contributed to writing and editing.

Competing interests. The contact author has declared that none of the authors has any competing interests.

Disclaimer. Publisher's note: Copernicus Publications remains neutral with regard to jurisdictional claims in published maps and institutional affiliations.

Acknowledgements. Dirk Nikolaus Karger, Loïc Pellissier, and Niklaus E. Zimmermann were funded by WSL internal grant exCHELSA, the 2019–2020 BiodivERsA joint call for research proposals, under the BiodivClim ERA-Net COFUND program, with the funding organizations Swiss National Science Foundation SNF (project: FeedBaCks, 193907) as well as the Swiss Data Science Project: SPEEDMIND. Philipp Brun, Dirk Nikolaus Karger, and Niklaus E. Zimmermann were supported by the Swiss Data Science Project: COMECO. Dirk Nikolaus Karger was funded by the ERA-Net BiodivERsA–Belmont Forum, with the national funder Swiss National Science Foundation (20BD21_184131), part of the 2018 joint BiodivERsA–Belmont Forum call (project "FutureWeb") as well as WSL internal grant ClimEx. We thank Babek Dabagchian for valuable support in data management and preparation.

Financial support. This research has been supported by the Swiss National Science Foundation (FeedBaCks project, grant no. 193907; FutureWeb project, grant no. 20BD21_184131).

Review statement. This paper was edited by David Carlson and reviewed by two anonymous referees.

References

Aguilos, M., Sun, G., Noormets, A., Domec, J.-C., McNulty, S., Gavazzi, M., Prajapati, P., Minick, K. J., Mitra, B., and King, J.: Ecosystem Productivity and Evapotranspiration Are Tightly Coupled in Loblolly Pine (Pinus taeda L.) Plantations along the Coastal Plain of the Southeastern U.S., Carbon and Water Cycles in Coastal Forests under Climate Change and Variability, Forests, 12, 1123, https://doi.org/10.3390/f12081123, 2021.

Alduchov, O. A. and Eskridge, R. E.: Improved Magnus Form Approximation of Saturation Vapor Pressure, J. Appl. Meteorol., 35, 601–609, https://doi.org/10.1175/1520-0450(1996)035<0601:IMFAOS>2.0.CO;2, 1996.

Allen, C. D., Macalady, A. K., Chenchouni, H., Bachelet, D., McDowell, N., Vennetier, M., Kitzberger, T., Rigling, A., Breshears, D. D., Hogg, E. H., Gonzalez, P., Fensham, R., Zhang, Z., Castro, J., Demidova, N., Lim, J.-H., Allard, G., Running, S. W., Semerci, A., and Cobb, N.: A global overview of drought and heat-induced tree mortality reveals emerging climate change risks for forests, For. Ecol. Manage., 259, 660–684, https://doi.org/10.1016/j.foreco.2009.09.001, 2010.

Allen, R. G., Pereira, L. S., Raes, D., and Smith, M.: Crop evapotranspiration – guidelines for computing crop water requirements, FAO Irrig. Drain. Pap., 56, ISBN 9251042195, 1998.

Anandhi, A.: Growing degree days – Ecosystem indicator for changing diurnal temperatures and their impact on corn growth stages in Kansas, Ecol. Indic., 61, 149–158, https://doi.org/10.1016/j.ecolind.2015.08.023, 2016.

Andrade, A. M. D., Michel, R. F. M., Bremer, U. F., Schaefer, C. E. G. R., and Simões, J. C.: Relationship between solar radiation and surface distribution of vegetation in Fildes Peninsula and Ardley Island, Maritime Antarctica, Int. J. Remote Sens., 39, 2238–2254, https://doi.org/10.1080/01431161.2017.1420937, 2018.

Araújo, M. B. and Rahbek, C.: How Does Climate Change Affect Biodiversity?, Science, 313, 1396–1397, https://doi.org/10.1126/science.1131758, 2006.

Arguez, A. and Vose, R. S.: The Definition of the Standard WMO Climate Normal: The Key to Deriving Alternative Climate Normals, Bull. Am. Meteorol. Soc., 92, 699–704, https://doi.org/10.1175/2010BAMS2955.1, 2011.

Bellard, C., Bertelsmeier, C., Leadley, P., Thuiller, W., and Courchamp, F.: Impacts of climate change on the future of biodiversity, Ecol. Lett., 15, 365–377, https://doi.org/10.1111/j.1461-0248.2011.01736.x, 2012.

Bobrowski, M., Weidinger, J., and Schickhoff, U.: Is New Always Better? Frontiers in Global Climate Datasets for Modeling Treeline Species in the Himalayas, Atmosphere (Basel), 12, 543, https://doi.org/10.3390/atmos12050543, 2021.

Böhner, J. and Antonic, O.: Land-Surface Parameters Specific to Topo-Climatology, in: Geomorphometry: Concepts, Software, Applications, 195–226, https://doi.org/10.1016/S0166-2481(08)00008-1, 2009.

Bojinski, S., Verstraete, M., Peterson, T. C., Richter, C., Simmons, A., and Zemp, M.: The Concept of Essential Climate Variables in Support of Climate Research, Applications, and Policy, Bull. Am. Meteorol. Soc., 95, 1431–1443, https://doi.org/10.1175/BAMS-D-13-00047.1, 2014.

Boucher, O., Servonnat, J., Albright, A. L., Aumont, O., Balkanski, Y., Bastrikov, V., Bekki, S., Bonnet, R., Bony, S., Bopp, L., Braconnot, P., Brockmann, P., Cadule, P., Caubel, A., Cheruy, F., Codron, F., Cozic, A., Cugnet, D., D'Andrea, F., Davini, P., Lavergne, C., Denvil, S., Deshayes, J., Devilliers, M., Ducharne, A., Dufresne, J., Dupont, E., Éthé, C., Fairhead, L., Falletti, L., Flavoni, S., Foujols, M., Gardoll, S., Gastineau, G., Ghattas, J., Grandpeix, J., Guenet, B., Guez, Lionel, E., Guilyardi, E., Guimberteau, M., Hauglustaine, D., Hourdin, F., Idelkadi, A., Joussaume, S., Kageyama, M., Khodri, M., Krinner, G., Lebas, N., Levavasseur, G., Lévy, C., Li, L., Lott, F., Lurton, T., Luyssaert, S., Madec, G., Madeleine, J., Maignan, F., Marchand, M., Marti, O., Mellul, L., Meurdesoif, Y., Mignot, J., Musat, I., Ottlé, C., Peylin, P., Planton, Y., Polcher, J., Rio, C., Rochetin, N., Rousset, C., Sepulchre, P., Sima, A., Swingedouw, D., Thiéblemont, R., Traore, A. K., Vancoppenolle, M., Vial, J., Vialard, J., Viovy, N., and Vuichard, N.: Presentation and Evaluation of the IPSL-CM6A-LR Climate Model, J. Adv. Model. Earth Syst.,

12, e2019MS002010, https://doi.org/10.1029/2019MS002010, 2020.

Brun, P., Zimmermann, N. E., Hari, C., Pellissier, L., and Karger, D. N.: CHELSA-BIOCLIM+ A novel set of global climate-related predictors at kilometre-resolution, EnviDat [data set], https://doi.org/10.16904/envidat.332, 2022.

Callaghan, T. V., Johansson, M., Brown, R. D., Groisman, P. Y., Labba, N., Radionov, V., Bradley, R. S., Blangy, S., Bulygina, O. N., Christensen, T. R., Colman, J. E., Essery, R. L. H., Forbes, B. C., Forchhammer, M. C., Golubev, V. N., Honrath, R. E., Juday, G. P., Meshcherskaya, A. V., Phoenix, G. K., Pomeroy, J., Rautio, A., Robinson, D. A., Schmidt, N. M., Serreze, M. C., Shevchenko, V. P., Shiklomanov, A. I., Shmakin, A. B., Sköld, P., Sturm, M., Woo, M., and Wood, E. F.: Multiple Effects of Changes in Arctic Snow Cover, Ambio, 40, 32–45, https://doi.org/10.1007/s13280-011-0213-x, 2011.

Cayton, H. L., Haddad, N. M., Gross, K., Diamond, S. E., and Ries, L.: Do growing degree days predict phenology across butterfly species?, Ecology, 96, 1473–1479, https://doi.org/10.1890/15-0131.1, 2015.

Conrad, O., Bechtel, B., Bock, M., Dietrich, H., Fischer, E., Gerlitz, L., Wehberg, J., Wichmann, V., and Böhner, J.: System for Automated Geoscientific Analyses (SAGA) v. 2.1.4, Geosci. Model Dev., 8, 1991–2007, https://doi.org/10.5194/gmd-8-1991-2015, 2015.

Daly, C., Taylor, G. H., and Gibson, W. P.: The PRISM approach to mapping precipitation and temperature, in: Proc 10th AMS Conf Appl. Climatol., 20–23, https://prism.oregonstate.edu/documents/pubs/1997appclim_PRISMapproach_daly.pdf (last access: 12 December 2022), 1997.

Danielson, J. J. and Gesch, D. B.: Global multi-resolution terrain elevation data 2010 (GMTED2010), Earth Resources Observation And Science (EROS) Center, https://doi.org/10.5066/F7J38R2N, 2011.

Datta, A., Schweiger, O., and Kühn, I.: Origin of climatic data can determine the transferability of species distribution models, 59, 61–76, https://doi.org/10.3897/neobiota.59.36299, 2020.

Dawson, T. E.: Fog in the California redwood forest: ecosystem inputs and use by plants, Oecologia, 117, 476–485, https://doi.org/10.1007/s004420050683, 1998.

Dunn, R. J. H.: HadISD version 3: monthly updates, Hadley Centre Technical Note, https://digital.nmla.metoffice.gov.uk/digitalFile_13890750-fb6f-42c7-92df-1c4504621fae/ (last access: last access: 12 December 2022), 2019.

Easterling, D. R., Meehl, G. A., Parmesan, C., Changnon, S. A., Karl, T. R., and Mearns, L. O.: Climate Extremes: Observations, Modeling, and Impacts, Science, 289, 2068–2074, https://doi.org/10.1126/science.289.5487.2068, 2000.

Easterling, D. R., Kunkel, K. E., Wehner, M. F., and Sun, L.: Detection and attribution of climate extremes in the observed record, Weather Clim. Extrem., 11, 17–27, https://doi.org/10.1016/j.wace.2016.01.001, 2016.

Elsen, P. R., Monahan, W. B., Dougherty, E. R., and Merenlender, A. M.: Keeping pace with climate change in global terrestrial protected areas, Sci. Adv., 6, eaay0814, https://doi.org/10.1126/sciadv.aay0814, 2020.

Evans, B. M., Walker, D. A., Benson, C. S., Nordstrand, E. A., and Petersen, G. W.: Spatial interrelationships between terrain, snow distribution and vegetation patterns at an arctic foothills site in Alaska, Ecography, 12, 270–278, https://doi.org/10.1111/j.1600-0587.1989.tb00846.x, 1989.

Eyring, V., Bony, S., Meehl, G. A., Senior, C. A., Stevens, B., Stouffer, R. J., and Taylor, K. E.: Overview of the Coupled Model Intercomparison Project Phase 6 (CMIP6) experimental design and organization, Geosci. Model Dev., 9, 1937–1958, https://doi.org/10.5194/gmd-9-1937-2016, 2016.

FAO: FAOCLIM 2: world-wide agroclimatic data, Environment and Natural Resources, Working paper No. 5 (CD-ROM), FAO [data set], https://www.fao.org/land-water/land/land-governance/land-resources-planning-toolbox/category/details/en/c/1028000/ (last access: 13 December 2022), 2001.

Fick, S. E. and Hijmans, R. J.: WorldClim 2: new 1 km spatial resolution climate surfaces for global land areas, Int. J. Climatol., 37, 4302–4315, https://doi.org/10.1002/joc.5086, 2017.

Fourcade, Y., Besnard, A. G., and Secondi, J.: Paintings predict the distribution of species, or the challenge of selecting environmental predictors and evaluation statistics, Glob. Ecol. Biogeogr., 27, 245–256, https://doi.org/10.1111/geb.12684, 2018.

Gholz, H. L.: Environmental Limits on Aboveground Net Primary Production, Leaf Area, and Biomass in Vegetation Zones of the Pacific Northwest, Ecology, 63, 469–481, https://doi.org/10.2307/1938964, 1982.

Grier, C. G. and Running, S. W.: Leaf Area of Mature Northwestern Coniferous Forests: Relation to Site Water Balance, Ecology, 58, 893–899, https://doi.org/10.2307/1936225, 1977.

Grossiord, C., Buckley, T. N., Cernusak, L. A., Novick, K. A., Poulter, B., Siegwolf, R. T. W., Sperry, J. S., and McDowell, N. G.: Plant responses to rising vapor pressure deficit, New Phytol., 226, 1550–1566, https://doi.org/10.1111/nph.16485, 2020.

Gutjahr, O., Putrasahan, D., Lohmann, K., Jungclaus, J. H., von Storch, J.-S., Brüggemann, N., Haak, H., and Stössel, A.: Max Planck Institute Earth System Model (MPI-ESM1.2) for the High-Resolution Model Intercomparison Project (HighResMIP), Geosci. Model Dev., 12, 3241–3281, https://doi.org/10.5194/gmd-12-3241-2019, 2019.

Hannah, L.: Protected Areas and Climate Change, Ann. N. Y. Acad. Sci., 1134, 201–212, https://doi.org/10.1196/annals.1439.009, 2008.

Hargreaves, G. H. and Samani, Z. A.: Reference Crop Evapotranspiration from Temperature, Appl. Eng. Agric., 1, 96–99, https://doi.org/10.13031/2013.26773, 1985.

Hartman, M. D., Parton, W. J., Derner, J. D., Schulte, D. K., Smith, W. K., Peck, D. E., Day, K. A., Del Grosso, S. J., Lutz, S., Fuchs, B. A., Chen, M., and Gao, W.: Seasonal grassland productivity forecast for the U.S. Great Plains using Grass-Cast, 11, e03280, https://doi.org/10.1002/ecs2.3280, 2020.

Hauser, G., Rais, O., Morán Cadenas, F., Gonseth, Y., Bouzelboudjen, M., and Gern, L.: Influence of climatic factors on Ixodes ricinus nymph abundance and phenology over a long-term monthly observation in Switzerland (2000–2014), Parasit. Vectors, 11, 289, https://doi.org/10.1186/s13071-018-2876-7, 2018.

Hay, L. E., Wilby, R. L., and Leavesley, G. H.: A Comparison Of Delta Change And Downscaled Gcm Scenarios For Three Mountainous Basins In The United States 1, JAWRA J. Am. Water Resour. Assoc., 36, 387–397, https://doi.org/10.1111/j.1752-1688.2000.tb04276.x, 2000.

Held, I. M., Guo, H., Adcroft, A., Dunne, J. P., Horowitz, L. W., Krasting, J., Shevliakova, E., Winton, M., Zhao, M., Bushuk,

M., Wittenberg, A. T., Wyman, B., Xiang, B., Zhang, R., Anderson, W., Balaji, V., Donner, L., Dunne, K., Durachta, J., Gauthier, P. P. G., Ginoux, P., Golaz, J. -C., Griffies, S. M., Hallberg, R., Harris, L., Harrison, M., Hurlin, W., John, J., Lin, P., Lin, S. -J., Malyshev, S., Menzel, R., Milly, P. C. D., Ming, Y., Naik, V., Paynter, D., Paulot, F., Ramaswamy, V., Reichl, B., Robinson, T., Rosati, A., Seman, C., Silvers, L. G., Underwood, S., and Zadeh, N.: Structure and Performance of GFDL's CM4.0 Climate Model, J. Adv. Model. Earth Syst., 11, 3691–3727, https://doi.org/10.1029/2019MS001829, 2019.

Hengl, T., de Jesus, J. M., MacMillan, R. A., Batjes, N. H., Heuvelink, G. B. M., Ribeiro, E., Samuel-Rosa, A., Kempen, B., Leenaars, J. G. B., Walsh, M. G., and Gonzalez, M. R.: SoilGrids1km – Global Soil Information Based on Automated Mapping, PLoS One, 9, e105992, https://doi.org/10.1371/journal.pone.0105992, 2014.

Hengl, T., Mendes de Jesus, J., Heuvelink, G. B. M., Ruiperez Gonzalez, M., Kilibarda, M., Blagotić, A., Shangguan, W., Wright, M. N., Geng, X., Bauer-Marschallinger, B., Guevara, M. A., Vargas, R., MacMillan, R. A., Batjes, N. H., Leenaars, J. G. B., Ribeiro, E., Wheeler, I., Mantel, S., and Kempen, B.: SoilGrids250m: Global gridded soil information based on machine learning, PLoS One, 12, e0169748, https://doi.org/10.1371/journal.pone.0169748, 2017.

Hersbach, H., Bell, B., Berrisford, P., Hirahara, S., Horányi, A., Muñoz-Sabater, J., Nicolas, J., Peubey, C., Radu, R., Schepers, D., Simmons, A., Soci, C., Abdalla, S., Abellan, X., Balsamo, G., Bechtold, P., Biavati, G., Bidlot, J., Bonavita, M., Chiara, G., Dahlgren, P., Dee, D., Diamantakis, M., Dragani, R., Flemming, J., Forbes, R., Fuentes, M., Geer, A., Haimberger, L., Healy, S., Hogan, R. J., Hólm, E., Janisková, M., Keeley, S., Laloyaux, P., Lopez, P., Lupu, C., Radnoti, G., Rosnay, P., Rozum, I., Vamborg, F., Villaume, S., and Thépaut, J.: The ERA5 global reanalysis, Q. J. Roy. Meteorol. Soc., 146, 1999–2049, https://doi.org/10.1002/qj.3803, 2020.

Hijmans, R. J.: raster: Geographic Data Analysis and Modeling, r-project [code], https://cran.r-project.org/package=raster (last access: 22 August 2019), 2019.

Hijmans, R. J., Cameron, S. E., Parra, J. L., Jones, P. G., and Jarvis, A.: Very high resolution interpolated climate surfaces for global land areas, Int. J. Climatol., 25, 1965–1978, https://doi.org/10.1002/joc.1276, 2005.

Hogg, E. H.: Temporal scaling of moisture and the forest-grassland boundary in western Canada, Agric. For. Meteorol., 84, 115–122, https://doi.org/10.1016/S0168-1923(96)02380-5, 1997.

Hogg, E. H., Michaelian, M., Hook, T. I., and Undershultz, M. E.: Recent climatic drying leads to age-independent growth reductions of white spruce stands in western Canada, Glob. Chang. Biol., 23, 5297–5308, https://doi.org/10.1111/gcb.13795, 2017.

Howden, S. M., Soussana, J.-F., Tubiello, F. N., Chhetri, N., Dunlop, M., and Meinke, H.: Adapting agriculture to climate change, Proc. Natl. Acad. Sci., 104, 19691–19696, https://doi.org/10.1073/pnas.0701890104, 2007.

Hufkens, K., Friedl, M. A., Keenan, T. F., Sonnentag, O., Bailey, A., O'Keefe, J., and Richardson, A. D.: Ecological impacts of a widespread frost event following early spring leaf-out, Glob. Chang. Biol., 18, 2365–2377, https://doi.org/10.1111/j.1365-2486.2012.02712.x, 2012.

Iio, A., Hikosaka, K., Anten, N. P. R., Nakagawa, Y., and Ito, A.: Global dependence of field-observed leaf area index in woody species on climate: a systematic review, Glob. Ecol. Biogeogr., 23, 274–285, https://doi.org/10.1111/geb.12133, 2014.

IPBES: The IPBES regional assessment report on biodiversity and ecosystem services for Europe and Central Asia., edited by: Rounsevell, M., Fischer, M., Torre-Marin Rando, A., and Mader, A., Secretariat of the Intergovernmental Science-Policy Platform on Biodiversity and Ecosystem Services, Bonn, Germany, 892 pp., https://doi.org/10.5281/zenodo.3237428, 2018.

IPCC: Renewable Energy Sources and Climate Change Mitigation: Special Report of the Intergovernmental Panel on Climate Change, edited by: Edenhofer, O., Pichs-Madruga, R., Sokona, Y., Seyboth, K., Matschoss, P., Kadner, S., Zwickel, T., Eickemeier, P., Hansen, G., Schlömer, S., and von Stechow, C., Cambridge University Press, Cambridge, ISBN 9781107607101, 2011.

IPCC: Climate Change 2022: Impacts, Adaptation, and Vulnerability. Contribution of Working Group II to the Sixth Assessment Report of the Intergovernmental Panel on Climate Change, edited by: Pörtner, H.-O., Roberts, D. C., Tignor, M., Poloczanska, E. S., Mintenbeck, K., Alegría, A., Craig, M., Langsdorf, S., Löschke, S., Möller, V., Okem, A., and Rama, B., Cambridge University Press, United Kingdom, https://doi.org/10.1017/9781009325844., 2022.

Irmak, S.: Evapotranspiration, in: Encyclopedia of Ecology, edited by: Jørgensen, S. E. and Fath, B. D., Academic Press, 1432–1438, https://doi.org/10.1016/B978-008045405-4.00270-6, 2008.

Karger, D. N., Conrad, O., Böhner, J., Kawohl, T., Kreft, H., Soria-Auza, R. W., Zimmermann, N. E., Linder, H. P., and Kessler, M.: Climatologies at high resolution for the earth's land surface areas, Sci. Data, 4, 170122, https://doi.org/10.1038/sdata.2017.122, 2017.

Karger, D. N., Schmatz, D. R., Dettling, G., and Zimmermann, N. E.: High-resolution monthly precipitation and temperature time series from 2006 to 2100, Sci. Data, 7, 248, https://doi.org/10.1038/s41597-020-00587-y, 2020.

Karger, D. N., Conrad, O., Böhner, J., Kawohl, T., Kreft, H., Soria-Auza, R. W., Zimmermann, N. E., Linder, H. P., and Kessler, M.: Climatologies at high resolution for the earth's land surface areas, EnviDat [data set], https://doi.org/10.16904/envidat.228.v2.1, 2021a.

Karger, D. N., Wilson, A. M., Mahony, C., Zimmermann, N. E., and Jetz, W.: Global daily 1 km land surface precipitation based on cloud cover-informed downscaling, Sci. Data, 8, 307, https://doi.org/10.1038/s41597-021-01084-6, 2021b.

Karger, D. N., Kessler, M., Lehnert, M., and Jetz, W.: Limited protection and ongoing loss of tropical cloud forest biodiversity and ecosystems worldwide, Nat. Ecol. Evol., 5, 854–862, https://doi.org/10.1038/s41559-021-01450-y, 2021c.

Karger, D. N., Lange, S., Hari, C., Reyer, C. P. O., Conrad, O., Zimmermann, N. E., and Frieler, K.: CHELSA-W5E5: Daily 1 km meteorological forcing data for climate impact studies, Earth Syst. Sci. Data Discuss. [preprint], https://doi.org/10.5194/essd-2022-367, in review, 2022.

Kawamiya, M., Hajima, T., Tachiiri, K., Watanabe, S., and Yokohata, T.: Two decades of Earth system modeling with an emphasis on Model for Interdisciplinary Research

on Climate (MIROC), Prog. Earth Planet. Sci., 7, 64, https://doi.org/10.1186/s40645-020-00369-5, 2020.

Knauer, J., El-Madany, T. S., Zaehle, S., and Migliavacca, M.: Bigleaf – An R package for the calculation of physical and physiological ecosystem properties from eddy covariance data, PLoS One, 13, e0201114, https://doi.org/10.1371/journal.pone.0201114, 2018.

Körner, C., Paulsen, J., and Spehn, E. M.: A definition of mountains and their bioclimatic belts for global comparisons of biodiversity data, Alp. Bot., 121, 73, https://doi.org/10.1007/s00035-011-0094-4, 2011.

Lange, S.: ISIMIP3b bias adjustment fact sheet, Inter-Sectoral Impact Model, Intercomparison Project, 40 pp., https://www.isimip.org/documents/413/ISIMIP3b_bias_adjustment_fact_sheet_Gnsz7CO.pdf (last access: 12 December 2022), 2021.

Larcher, W.: Ökophysiologie der Pflanzen: Leben und Stressbewältigung der Pflanzen in ihrer Umwelt, 5th edn., Verlag Eugen Ulmer, Stuttgart, 394 pp., ISBN 3825280748, 1994.

Leng, G. and Hall, J.: Crop yield sensitivity of global major agricultural countries to droughts and the projected changes in the future, Sci. Total Environ., 654, 811–821, https://doi.org/10.1016/j.scitotenv.2018.10.434, 2019.

Lenihan, J. M.: Ecological response surfaces for North American boreal tree species and their use in forest classification, J. Veg. Sci., 4, 667–680, https://doi.org/10.2307/3236132, 1993.

Levins, R.: The Strategy Of Model Building In Population Biology, Am. Sci., 54, 421–431, 1966.

Lieth, H.: Modeling the Primary Productivity of the World, in: Primary Productivity of the Biosphere, Springer, vol. 14, 237–263, https://doi.org/10.1007/978-3-642-80913-2_12, 1975.

Liu, W., Ye, T., Jägermeyr, J., Müller, C., Chen, S., Liu, X., and Shi, P.: Future climate change significantly alters interannual wheat yield variability over half of harvested areas, Environ. Res. Lett., 16, 094045, https://doi.org/10.1088/1748-9326/ac1fbb, 2021.

Masia, S., Trabucco, A., Spano, D., Snyder, R. L., Sušnik, J., and Marras, S.: A modelling platform for climate change impact on local and regional crop water requirements, Agric. Water Manag., 255, 107005, https://doi.org/10.1016/j.agwat.2021.107005, 2021.

Maussion, F., Scherer, D., Finkelnburg, R., Richters, J., Yang, W., and Yao, T.: WRF simulation of a precipitation event over the Tibetan Plateau, China – an assessment using remote sensing and ground observations, Hydrol. Earth Syst. Sci., 15, 1795–1817, https://doi.org/10.5194/hess-15-1795-2011, 2011.

Maussion, F., Scherer, D., Mölg, T., Collier, E., Curio, J., and Finkelnburg, R.: Precipitation Seasonality and Variability over the Tibetan Plateau as Resolved by the High Asia Reanalysis, J. Clim., 27, 1910–1927, https://doi.org/10.1175/JCLI-D-13-00282.1, 2014.

Monteith, J. L.: Evaporation and environment, Symp. Soc. Exp. Biol., 19, 205–234, 1965.

Muñoz Sabater, J.: ERA5-Land monthly averaged data from 1981 to present, Copernicus Climate Change Service (C3S) Climate Data Store (CDS) [data set], https://doi.org/10.24381/cds.68d2bb30, 2019.

Muñoz-Sabater, J.: ERA5-Land monthly averaged data from 1950 to 1980, Copernicus Climate Change Service (C3S) Climate Data Store (CDS) [data set], https://doi.org/10.24381/cds.68d2bb30, 2021.

Neilson, R. P.: A Model for Predicting Continental-Scale Vegetation Distribution and Water Balance, Ecol. Appl., 5, 362–385, https://doi.org/10.2307/1942028, 1995.

Nemani, R. R., Keeling, C. D., Hashimoto, H., Jolly, W. M., Piper, S. C., Tucker, C. J., Myneni, R. B., and Running, S. W.: Climate-Driven Increases in Global Terrestrial Net Primary Production from 1982 to 1999, Science, 300, 1560–1563, https://doi.org/10.1126/science.1082750, 2003.

Nobel, P. S.: Wind as an Ecological Factor, in: Physiological Plant Ecology I, Springer Berlin Heidelberg, Berlin, Heidelberg, vol. 12/A, 475–500, https://doi.org/10.1007/978-3-642-68090-8_16, 1981.

O'Neill, B. C., Kriegler, E., Riahi, K., Ebi, K. L., Hallegatte, S., Carter, T. R., Mathur, R., and van Vuuren, D. P.: A new scenario framework for climate change research: the concept of shared socioeconomic pathways, Clim. Change, 122, 387–400, https://doi.org/10.1007/s10584-013-0905-2, 2014.

O'Neill, B. C., Tebaldi, C., van Vuuren, D. P., Eyring, V., Friedlingstein, P., Hurtt, G., Knutti, R., Kriegler, E., Lamarque, J.-F., Lowe, J., Meehl, G. A., Moss, R., Riahi, K., and Sanderson, B. M.: The Scenario Model Intercomparison Project (ScenarioMIP) for CMIP6, Geosci. Model Dev., 9, 3461–3482, https://doi.org/10.5194/gmd-9-3461-2016, 2016.

O'Neill, B. C., Kriegler, E., Ebi, K. L., Kemp-Benedict, E., Riahi, K., Rothman, D. S., van Ruijven, B. J., van Vuuren, D. P., Birkmann, J., Kok, K., Levy, M., and Solecki, W.: The roads ahead: Narratives for shared socioeconomic pathways describing world futures in the 21st century, Glob. Environ. Chang., 42, 169–180, https://doi.org/10.1016/j.gloenvcha.2015.01.004, 2017.

Ooms, J.: magick: Advanced Graphics and Image-Processing in R, magick [code], https://CRAN.R-project.org/package=magick (last access: 12 December 2022), 2020.

Ouisse, T., Bonte, D., Lebouvier, M., Hendrickx, F., and Renault, D.: The importance of relative humidity and trophic resources in governing ecological niche of the invasive carabid beetle Merizodus soledadinus in the Kerguelen archipelago, J. Insect Physiol., 93–94, 42–49, https://doi.org/10.1016/j.jinsphys.2016.08.006, 2016.

Paulsen, J. and Körner, C.: A climate-based model to predict potential treeline position around the globe, Alp. Bot., 124, 1–12, https://doi.org/10.1007/s00035-014-0124-0, 2014.

Pebesma, E. J. and Bivand, R. S.: Classes and methods for spatial data in {R}, R News, 5, 9–13, 2005.

Pollock, L. J., Thuiller, W., and Jetz, W.: Large conservation gains possible for global biodiversity facets, Nature, 546, 141–144, https://doi.org/10.1038/nature22368, 2017.

Prentice, I. C., Cramer, W., Harrison, S. P., Leemans, R., Monserud, R. A., and Solomon, A. M.: Special Paper: A Global Biome Model Based on Plant Physiology and Dominance, Soil Properties and Climate, J. Biogeogr., 19, 117, https://doi.org/10.2307/2845499, 1992.

Pryor, S. C. and Hahmann, A. N.: Downscaling Wind, in: Oxford Research Encyclopedia of Climate Science, Oxford University Press, https://doi.org/10.1093/acrefore/9780190228620.013.730, 2019.

R Development Core Team: R: A Language and Environment for Statistical Computing, http://www.r-project.org (last access: 12 December 2022), 2008.

Santini, M., Noce, S., Antonelli, M., and Caporaso, L.: Complex drought patterns robustly explain global yield loss for major crops, Sci. Rep., 12, 5792, https://doi.org/10.1038/s41598-022-09611-0, 2022.

Schimel, D. S.: Terrestrial ecosystems and the carbon cycle, Glob. Chang. Biol., 1, 77–91, https://doi.org/10.1111/j.1365-2486.1995.tb00008.x, 1995.

Schultz, J.: The Ecozones of the World, The Ecological Divisions of the Geosphere, Springer Berlin Heidelberg, Berlin, Heidelberg, https://doi.org/10.1007/3-540-28527-X, 2005.

Sellar, A. A., Jones, C. G., Mulcahy, J. P., Tang, Y., Yool, A., Wiltshire, A., O'Connor, F. M., Stringer, M., Hill, R., Palmieri, J., Woodward, S., Mora, L., Kuhlbrodt, T., Rumbold, S. T., Kelley, D. I., Ellis, R., Johnson, C. E., Walton, J., Abraham, N. L., Andrews, M. B., Andrews, T., Archibald, A. T., Berthou, S., Burke, E., Blockley, E., Carslaw, K., Dalvi, M., Edwards, J., Folberth, G. A., Gedney, N., Griffiths, P. T., Harper, A. B., Hendry, M. A., Hewitt, A. J., Johnson, B., Jones, A., Jones, C. D., Keeble, J., Liddicoat, S., Morgenstern, O., Parker, R. J., Predoi, V., Robertson, E., Siahaan, A., Smith, R. S., Swaminathan, R., Woodhouse, M. T., Zeng, G., and Zerroukat, M.: UKESM1: Description and Evaluation of the U.K. Earth System Model, J. Adv. Model. Earth Syst., 11, 4513–4558, https://doi.org/10.1029/2019MS001739, 2019.

Seneviratne, S. I., Easterling, D., Goodess, C. M., Kanae, S., Kossin, J., Luo, Y., Marengo, J., McInnes, K., Rahimi, M., Reichstein, M., Sorteberg, A., Vera, C., and Zhang, X.: Changes in climate extremes and their impacts on the natural physical environment, in: Managing the Risks of Extreme Events and Disasters to Advance Climate Change Adaptation, edited by: Field, C. B., Barros, V., Stocker, T. F., Qin, D., Dokken, D. J., Ebi, K. L., Mastrandrea, M. D., Mach, K. J., Plattner, G.-K., Allen, S. K., Tignor, M., and Midgley, P. M., A Special Report of Working Groups I and II of the Intergovernmental Panel on Climate Change (IPCC), Cambridge, UK and New York, NY, USA, 109–230, https://doi.org/10.7916/d8-6nbt-s431, 2012.

Singer, M. B., Asfaw, D. T., Rosolem, R., Cuthbert, M. O., Miralles, D. G., MacLeod, D., Quichimbo, E. A., and Michaelides, K.: Hourly potential evapotranspiration at 0.1° resolution for the global land surface from 1981-present, Sci. Data, 8, 224, https://doi.org/10.1038/s41597-021-01003-9, 2021.

Skamarock, W. C. and Klemp, J. B.: A time-split nonhydrostatic atmospheric model for weather research and forecasting applications, J. Comput. Phys., 227, 3465–3485, https://doi.org/10.1016/j.jcp.2007.01.037, 2008.

Sloat, L. L., Davis, S. J., Gerber, J. S., Moore, F. C., Ray, D. K., West, P. C., and Mueller, N. D.: Climate adaptation by crop migration, Nat. Commun., 11, 1243, https://doi.org/10.1038/s41467-020-15076-4, 2020.

Sonntag, D.: Important new values of the physical constants of 1986, vapor pressure formulations based on the ITS-90 and psychrometric formulae, Z. Meteorol., 70, 340–344, 1990.

Sparks, A. H., Hengl, T., and Nelson, A.: GSODR: Global Summary Daily Weather Data in R, J. Open Source Softw., 2, 177, https://doi.org/10.21105/joss.00177, 2017.

Suwal, M. K., Huettmann, F., Regmi, G. R., and Vetaas, O. R.: Parapatric subspecies of Macaca assamensis show a marginal overlap in their predicted potential distribution: Some elaborations for modern conservation management, Ecol. Evol., 8, 9712–9727, https://doi.org/10.1002/ece3.4405, 2018.

Thuiller, W., Lavorel, S., Araújo, M. B., Sykes, M. T., and Prentice, I. C.: Climate change threats to plant diversity in Europe, Proc. Natl. Acad. Sci., 102, 8245–8250, https://doi.org/10.1073/pnas.0409902102, 2005.

Thuiller, W., Guéguen, M., Renaud, J., Karger, D. N., and Zimmermann, N. E.: Uncertainty in ensembles of global biodiversity scenarios, Nat. Commun., 10, 1446, https://doi.org/10.1038/s41467-019-09519-w, 2019.

Global Surface Summary of Day (GSOD): Index of /data/global-summary-of-the-day, NOAA [data set], https://www.ncei.noaa.gov/data/global-summary-of-the-day/, last access: 15 October 2022.

Weibull, W.: A Statistical Distribution Function of Wide Applicability, J. Appl. Mech., 18, 293–297, https://doi.org/10.1115/1.4010337, 1951.

Willis, K. J. and Bhagwat, S. A.: Biodiversity and Climate Change, Science, 326, 806–807, https://doi.org/10.1126/science.1178838, 2009.

WMO: Guide to Instruments and Methods of Observation, 8th edn., World Meteorological Organization, Geneva, 548 pp., ISBN 9789263100085, 2018.

Woodward, F. I.: Climate and plant distribution, Cambridge University Press, Cambridge, 192 pp., ISBN 9780521282147, 1987.

Yukimoto, S., Kawai, H., Koshiro, T., Oshima, N., Yoshida, K., Urakawa, S., Tsujino, H., Deushi, M., Tanaka, T., Hosaka, M., Yabu, S., Yoshimura, H., Shindo, E., Mizuta, R., Obata, A., Adachi, Y., and Ishii, M.: The Meteorological Research Institute Earth System Model Version 2.0, MRI-ESM2.0: Description and Basic Evaluation of the Physical Component, J. Meteorol. Soc. Japan. Ser. II, 97, 931–965, https://doi.org/10.2151/jmsj.2019-051, 2019.

Zeng, Z., Ziegler, A. D., Searchinger, T., Yang, L., Chen, A., Ju, K., Piao, S., Li, L. Z. X., Ciais, P., Chen, D., Liu, J., Azorin-Molina, C., Chappell, A., Medvigy, D., and Wood, E. F.: A reversal in global terrestrial stilling and its implications for wind energy production, Nat. Clim. Chang., 9, 979–985, https://doi.org/10.1038/s41558-019-0622-6, 2019.

Zhang, K., Bosch-Serra, A. D., Boixadera, J., and Thompson, A. J.: Investigation of Water Dynamics and the Effect of Evapotranspiration on Grain Yield of Rainfed Wheat and Barley under a Mediterranean Environment: A Modelling Approach, PLoS One, 10, e0131360, https://doi.org/10.1371/journal.pone.0131360, 2015.

Zhang, T.: Influence of the seasonal snow cover on the ground thermal regime: An overview, Rev. Geophys., 43, 2004RG000157, https://doi.org/10.1029/2004RG000157, 2005.

Ziese, M., Rauthe-Schöch, A., Becker, A., Finger, P., Meyer-Christoffer, A., and Schneider, U.: GPCC Full Data Daily Version.2018 at 1.0°: Daily Land-Surface Precipitation from Rain-Gauges built on GTS-based and Historic Data, https://doi.org/10.5676/DWD_GPCC/FD_D_V2018_100, 2018.

Zomer, R. J., Xu, J., and Trabucco, A.: Version 3 of the Global Aridity Index and Potential Evapotranspiration Database, Sci. Data, 9, 409, https://doi.org/10.1038/s41597-022-01493-1, 2022.

Zscheischler, J., Westra, S., van den Hurk, B. J. J. M., Seneviratne, S. I., Ward, P. J., Pitman, A., AghaKouchak, A., Bresch,

D. N., Leonard, M., Wahl, T., and Zhang, X.: Future climate risk from compound events, Nat. Clim. Chang., 8, 469–477, https://doi.org/10.1038/s41558-018-0156-3, 2018.